



## The G0 experiment: Apparatus for parity-violating electron scattering measurements at forward and backward angles

D. Androić<sup>t</sup>, D.S. Armstrong<sup>c</sup>, J. Arvieux<sup>e,1</sup>, R. Asaturyan<sup>u,1</sup>, T.D. Averett<sup>c</sup>, S.L. Bailey<sup>c,2</sup>, G. Batigne<sup>g,3</sup>, D.H. Beck<sup>m,\*</sup>, E.J. Beise<sup>p</sup>, J. Benesch<sup>k</sup>, F. Benmokhtar<sup>b,p,4</sup>, L. Bimbot<sup>e</sup>, J. Birchall<sup>o</sup>, A. Biselli<sup>b,5</sup>, P. Bosted<sup>k</sup>, H. Breuer<sup>p</sup>, P. Brindza<sup>k</sup>, C.L. Capuano<sup>c</sup>, R.D. Carlini<sup>k</sup>, R. Carr<sup>a</sup>, N. Chant<sup>p</sup>, Y.-C. Chao<sup>k,6</sup>, R. Clark<sup>b,7</sup>, A. Coppens<sup>o,8</sup>, S.D. Covrig<sup>a,9</sup>, A. Cowley<sup>p,10</sup>, D. Dale<sup>n,11</sup>, C.A. Davis<sup>l</sup>, C. Ellis<sup>p</sup>, W.R. Falk<sup>o</sup>, H. Fenker<sup>k</sup>, J.M. Finn<sup>c,1</sup>, T. Forest<sup>h,11</sup>, G. Franklin<sup>b</sup>, R. Frascaria<sup>e</sup>, C. Furget<sup>g</sup>, D. Gaskell<sup>k</sup>, M.T.W. Gericke<sup>o</sup>, J. Grames<sup>k</sup>, K.A. Griffioen<sup>c</sup>, K. Grimm<sup>c,12</sup>, G. Guillard<sup>g,13</sup>, B. Guillon<sup>g,14</sup>, H. Guler<sup>e,15</sup>, K. Gustafsson<sup>a,16</sup>, L. Hannelius<sup>a</sup>, J. Hansknecht<sup>k</sup>, R.D. Hasty<sup>m,17</sup>, A.M. Hawthorne Allen<sup>r,18</sup>, T. Horn<sup>p,19</sup>, T.M. Ito<sup>a,20</sup>, K. Johnston<sup>h</sup>, M. Jones<sup>k</sup>, P. Kammel<sup>m,21</sup>, R. Kazimi<sup>k</sup>, P.M. King<sup>m,p,j</sup>, A. Kolarkar<sup>n,22</sup>, E. Korkmaz<sup>q</sup>, W. Korsch<sup>n</sup>, S. Kox<sup>g</sup>, J. Kuhn<sup>b,23</sup>, J. Lachniet<sup>b</sup>, R. Laszewski<sup>m</sup>, L. Lee<sup>l,o</sup>, J. Lenoble<sup>e</sup>, E. Liatard<sup>g</sup>, J. Liu<sup>a,p,24</sup>, A. Lung<sup>k</sup>, G.A. MacLachlan<sup>i,25</sup>, J. Mammei<sup>r,26</sup>, D. Marchand<sup>e</sup>, J.W. Martin<sup>a,s</sup>, D.J. Mack<sup>k</sup>, K.W. McFarlane<sup>d</sup>, D.W. McKee<sup>i,27</sup>, R.D. McKeown<sup>a,9</sup>, F. Merchez<sup>g</sup>, M. Mihovilovic<sup>f</sup>, A. Micherdzinska<sup>s,25</sup>, H. Mkrtchyan<sup>u</sup>, B. Moffit<sup>c,9</sup>, M. Morlet<sup>e</sup>, M. Muether<sup>m,28</sup>, J. Musson<sup>k</sup>, K. Nakahara<sup>m,29</sup>, R. Neveling<sup>m,30</sup>, S. Niccolai<sup>e</sup>, D. Nilsson<sup>m,31</sup>, S. Ong<sup>e</sup>, S.A. Page<sup>o</sup>, V. Papavassiliou<sup>i</sup>, S.F. Pate<sup>i</sup>, S.K. Phillips<sup>c,32</sup>, P. Pillot<sup>g,3</sup>, M.L. Pitt<sup>r</sup>, M. Poelker<sup>k</sup>, T.A. Porcelli<sup>q</sup>, G. Quéméner<sup>g,16</sup>, B.P. Quinn<sup>b</sup>, W.D. Ramsay<sup>l,o</sup>, A.W. Rauf<sup>o,33</sup>, J.-S. Real<sup>g</sup>, T. Ries<sup>l</sup>, J. Roche<sup>c,k,j</sup>, P. Roos<sup>p</sup>, G.A. Rutledge<sup>o,34</sup>, J. Schaub<sup>i,35</sup>, J. Secret<sup>c,36</sup>, T. Seva<sup>t</sup>, N. Simicevic<sup>h</sup>, G.R. Smith<sup>k</sup>, D.T. Spayde<sup>m,37</sup>, S. Stepanyan<sup>u</sup>, M. Stutzman<sup>k</sup>, R. Suleiman<sup>r,9</sup>, V. Tadevosyan<sup>u</sup>, R. Tieulent<sup>g,38</sup>, J. van de Wiele<sup>e</sup>, W.T.H. van Oers<sup>o</sup>, M. Versteegen<sup>g,39</sup>, E. Voutier<sup>g</sup>, W.F. Vulcan<sup>k</sup>, S.P. Wells<sup>h</sup>, G. Warren<sup>k</sup>, S.E. Williamson<sup>m</sup>, R.J. Woo<sup>o</sup>, S.A. Wood<sup>k</sup>, C. Yan<sup>k</sup>, J. Yun<sup>r</sup>, V. Zeps<sup>n,40</sup>

<sup>a</sup> Kellogg Radiation Laboratory, California Institute of Technology, 1201 California Blvd, Pasadena, CA 91125, USA

<sup>b</sup> Department of Physics, Carnegie Mellon University, Pittsburgh, PA 15213, USA

<sup>c</sup> Department of Physics, College of William and Mary, Williamsburg, VA 23187, USA

<sup>d</sup> Department of Physics, Hampton University, Hampton, VA 23668, USA

<sup>e</sup> Institut de Physique Nucleaire d'Orsay, F-91406 ORSAY-Cedex, France

<sup>f</sup> Joz'wiedehatef Stefan Institute, 1000 Ljubljana, Slovenia

<sup>g</sup> LPSC, Université Joseph Fourier Grenoble 1, CNRS/IN2P3, Institut Polytechnique de Grenoble, Grenoble, France

<sup>h</sup> Department of Physics, Louisiana Tech University, P.O. Box 3169 T.S., Ruston, LA 71272, USA

<sup>i</sup> Department of Physics, New Mexico State University, Las Cruces, NM 88003, USA

<sup>j</sup> Department of Physics and Astronomy, Ohio University, Athens, OH 45701, USA

<sup>k</sup> Thomas Jefferson National Accelerator Facility, 12000 Jefferson Avenue, Newport News, VA 23606, USA

<sup>l</sup> TRIUMF, 4004 Westbrook Mall, Vancouver, BC, Canada V6T 2A3

<sup>m</sup> Loomis Laboratory of Physics, University of Illinois, 1110 West Green Street, Urbana, IL 61801, USA

<sup>n</sup> Department of Physics and Astronomy, University of Kentucky, Lexington, KY 40506, USA

<sup>o</sup> Department of Physics, University of Manitoba, Winnipeg, Manitoba, Canada R3T 2N2

<sup>p</sup> Department of Physics, University of Maryland, College Park, MD 20472, USA

<sup>q</sup> Department of Physics, University of Northern British Columbia, 3333, University Way, Prince George, BC, Canada V2N 4Z9

<sup>r</sup> Department of Physics, Virginia Tech, Blacksburg, VA 24061, USA

<sup>s</sup> Department of Physics, University of Winnipeg, Winnipeg, MB, Canada R3B 2E9

<sup>t</sup> Department of Physics, University of Zagreb, Zagreb HR-41001, Croatia

<sup>u</sup> Yerevan Physics Institute, Alikhanian Brothers 2, Yerevan 375036, Armenia

\* Corresponding author. Tel.: +1 217 244 7994.

E-mail address: [dhbeck@illinois.edu](mailto:dhbeck@illinois.edu) (D.H. Beck).

<sup>1</sup> Deceased.

<sup>2</sup> Current address: Center for Health Policy/Center for Primary Care and Outcomes Research, Stanford University, Stanford, CA.

<sup>3</sup> Current address: Laboratoire Subatech, Nantes, France.

## ARTICLE INFO

## Article history:

Received 11 October 2010

Received in revised form

18 April 2011

Accepted 19 April 2011

Available online 29 April 2011

## Keywords:

Magnetic spectrometer  
Liquid hydrogen target  
Polarized electron beam  
Parity-violation  
Electron scattering

## ABSTRACT

In the G0 experiment, performed at Jefferson Lab, the parity-violating elastic scattering of electrons from protons and quasi-elastic scattering from deuterons is measured in order to determine the neutral weak currents of the nucleon. Asymmetries as small as 1 part-per-million in the scattering of a polarized electron beam are determined using a dedicated apparatus. It consists of specialized beam monitoring and control systems, a cryogenic hydrogen (or deuterium) target, and a superconducting, toroidal magnetic spectrometer equipped with plastic scintillation and aerogel Cherenkov detectors, as well as fast readout electronics for the measurement of individual events. The overall design and performance of this experimental system is discussed.

© 2011 Elsevier B.V. All rights reserved.

<sup>4</sup> Current address: Department of Physics, Computer Science and Engineering, Christopher Newport University, Newport News, VA, USA.

<sup>5</sup> Current address: Department of Physics, Fairfield University, Fairfield, CT, USA.

<sup>6</sup> Current address: TRIUMF, Vancouver, BC, Canada.

<sup>7</sup> Current address: Department of Physics and Astronomy, University of Pittsburgh, Pittsburgh, PA, USA.

<sup>8</sup> Current address: Department of Physics, Carleton University, Ottawa, ON, Canada.

<sup>9</sup> Current address: Jefferson Lab, Newport News, VA, USA.

<sup>10</sup> Current address: Department of Physics, Stellenbosch University, Stellenbosch, South Africa.

<sup>11</sup> Current address: Department of Physics, Idaho State University, Pocatello, ID, USA.

<sup>12</sup> Current address: Department of Physics, Louisiana Tech University, Ruston, LA, USA.

<sup>13</sup> Current address: LPC, Clermont-Ferrand, France.

<sup>14</sup> Current address: LPC-Caen, Caen, France.

<sup>15</sup> Current address: Laboratoire Leprince-Ringuet, Ecole Polytechnique, Palaiseau, France.

<sup>16</sup> Current address: National Board of Patents and Registration, Helsinki, Finland.

<sup>17</sup> Current address: Illinois Emergency Management Agency, Springfield, IL, USA.

<sup>18</sup> Current address: Department of Physica Sciences, Concord University, Athens, WV, USA.

<sup>19</sup> Current address: Department of Physics, The Catholic University of America, Washington, DC, USA.

<sup>20</sup> Current address: Los Alamos National Laboratory, Los Alamos, NM, USA.

<sup>21</sup> Current address: University of Washington, Seattle, WA, USA.

<sup>22</sup> Current address: Department of Physics, Boston University, Boston, MA, USA.

<sup>23</sup> Current address: Greens Farms Academy, Fairfield, CT, USA.

<sup>24</sup> Current address: Department of Physics, Shanghai Jiao Tong University, Shanghai, China.

<sup>25</sup> Current address: Department of Physics, The George Washington University, Washington, DC, USA.

<sup>26</sup> Current address: Department of Physics, University of Massachusetts, Amherst, MA, USA.

<sup>27</sup> Current address: Department of Physics, Kansas State University, Manhattan, KS, USA.

<sup>28</sup> Current address: Fermilab, Batavia, IL, USA.

<sup>29</sup> Current address: Department of Physics, University of Maryland, College Park, MD, USA.

<sup>30</sup> Current address: iThemba Labs, Stellenbosch University, Stellenbosch, South Africa.

<sup>31</sup> Current address: Visma Spcs AB, Växjö, Sweden.

<sup>32</sup> Current address: Department of Physics, University of New Hampshire, Durham, NH, USA.

<sup>33</sup> Current address: COMSATS, Islamabad, Pakistan.

<sup>34</sup> Current address: SAIC, San Diego, CA, USA.

<sup>35</sup> Current address: Department of Physics and Astronomy, Valparaiso University, Valparaiso, IN, USA.

<sup>36</sup> Current address: Department of Chemistry and Physics, Armstrong Atlantic State University, Savannah, GA, USA.

<sup>37</sup> Current address: Department of Physics, Hendrix College, Conway, AR, USA.

<sup>38</sup> Current address: IPNL, Lyon, France.

<sup>39</sup> Current address: Department of Physics, Université de Bordeaux, Bordeaux, France.

<sup>40</sup> Current address: Department of Physics and Astronomy, Bluegrass Community and Technical College, Lexington, KY, USA.

## 1. Introduction

In the G0 experiment, the parity-violating elastic scattering of electrons from protons and quasi-elastic scattering from deuterons is measured in order to determine the neutral weak currents of the nucleon [1]. By combining information from the ordinary electromagnetic form factors of the nucleon with the analogous quantities that define their neutral weak currents, the contributions of the three lightest flavors of quark to these currents can be extracted [2,3]. The parity-violating contribution to elastic scattering from the nucleon, in the momentum transfer region of interest, is of order  $10^{-5}$  times the electromagnetic contribution, and the goal is to measure it with an uncertainty of a few percent of its value. The G0 experiment in Hall C at the Thomas Jefferson National Accelerator Facility (Jefferson Lab) in Newport News, VA utilizes a specialized apparatus to perform these measurements.

The experimental quantity of interest is the parity-violating asymmetry—the relative difference in the scattering probability of right- and left-handed (longitudinally polarized) electrons

$$A_{PV} = \frac{\sigma_+ - \sigma_-}{\sigma_+ + \sigma_-}. \quad (1)$$

This asymmetry is sensitive to the interference of the electromagnetic and neutral weak currents, hence contains products of electromagnetic and neutral weak form factors. The experiment is carried out in two parts, corresponding to two different kinematic conditions: electrons scattered in the forward and backward hemispheres, respectively. These two measurements, similar to the measurements in the standard Rosenbluth separation method in ordinary electron scattering, allow us to isolate two linear combinations of form factor products in the asymmetry

$$A_{PV} = \frac{[-G_F Q^2] \varepsilon G_E^{\gamma} G_E^Z + \tau G_M^{\gamma} G_M^Z - (1 - 4 \sin^2 \theta_W) \varepsilon' G_M^{\gamma} G_A^e}{4\sqrt{2}\pi\alpha} \frac{1}{\varepsilon(G_E^{\gamma})^2 + \tau(G_M^{\gamma})^2} \quad (2)$$

where  $\alpha$  and  $G_F$  are the electromagnetic and weak coupling constants,  $Q^2 > 0$  is the four-momentum transfer,  $\theta$  is the laboratory electron scattering angle,  $G_E^{\gamma}$  and  $G_M^{\gamma(Z)}$  are the electromagnetic (analogous neutral weak) charge and magnetic proton form factors,  $G_A^e$  is the proton axial form factor as seen in parity-violating electron scattering (related to  $G_A$  measured in elastic neutrino scattering and the nucleon anapole moment [1]), and

$$\tau = \frac{Q^2}{4M_N^2}$$

$$\varepsilon = \frac{1}{1 + 2(1 + \tau)\tan^2 \frac{\theta}{2}}$$

and

$$\varepsilon' = \sqrt{\tau(1 + \tau)(1 - \varepsilon^2)} \quad (3)$$

are standard kinematic quantities depending on the nucleon mass  $M_N$ . The two products so determined are nominally  $G_E^V G_E^Z$  and  $G_M^V G_M^Z$ . The third term in the numerator of Eq. (2), however, also contributes to the measured asymmetry, especially at backward scattering angles where  $\varepsilon'$  is large. The axial form factor  $G_A^E$  is of considerable interest in and of itself. A third measurement is therefore needed in order to isolate this term. This can be done by measuring quasi-elastic scattering from the deuteron at backward electron scattering angles and utilizing the charge symmetry [4] of the proton-neutron system

$$G^{p,n} = \frac{1}{2} (G^{T=0} \pm G^{T=1}) \quad (4)$$

where  $T$  is the nucleon isospin. These three measurements, together with the known electromagnetic form factors of the nucleon,  $G^V$ , allow us to obtain separately contributions of the three lightest quark flavors to the structure of the nucleon [1]. The first results of both parts of the experiment are published elsewhere [5,6].

The primary design consideration in the experiment is the small asymmetry to be measured. In addition, capabilities for forward and backward angle measurements with both hydrogen and deuterium targets are required. This leads to a design with a large-acceptance magnetic spectrometer that detects recoil protons for the forward angle measurement and electrons for the backward angle measurements, and includes capabilities for background rejection. Measurements at the forward angle require more novel techniques, hence the paper has more emphasis on that aspect of the apparatus and technique. The following discussion opens with a more detailed assessment of the design requirements, and is followed by sections on the individual subsystems: beam, target, magnet, detectors, readout and data-acquisition electronics. It should be noted that in such experiments control and monitoring of the beam is critical, therefore we also include a section on the relevant aspects of the accelerator system. More detailed descriptions of the target [7] and forward angle electronics [8] can be found elsewhere.

## 2. Summary of design requirements

### 2.1. General considerations

The asymmetries to be measured over the desired range of momentum transfers,  $0.1 < Q^2 < 1 \text{ GeV}^2$ , range from about 1 part-per-million (ppm) for the lowest  $Q^2$  forward measurement to about

40 ppm for the highest  $Q^2$  at backward angles (all asymmetries, as defined above, are negative). In order to measure these asymmetries with a relative precision of a few percent, statistical and systematic uncertainties must be very small (generally  $< 10^{-7}$ ).

The statistical uncertainty ( $\Delta A = 1/\sqrt{N_{tot}}$ , where  $N_{tot}$  is the total number of detected events) is attained using a combination of high luminosity and large solid angle acceptance. For the G0 experiment, beam currents of 20–60  $\mu\text{A}$  are used with a 20 cm liquid hydrogen (or deuterium) target for a luminosity of about  $1-3 \times 10^{38} \text{ cm}^{-2} \text{ s}^{-1}$ . The spectrometer has a solid angle acceptance of roughly 0.9 sr and corresponding momentum acceptances for elastic scattering. These acceptances comprise the full range of momentum transfer in the forward measurement, and that corresponding to a single momentum transfer in the backward measurement as described below. Further, the acceptance is flat along the length of the target and the optics are such that particles from different points along the target are focused to the same location on the focal surface (see Fig. 1).

The small systematic uncertainties achieved derive mainly from the photocathode source of polarized electrons in the accelerator gun; the remarkably precise control of the intensity, pointing and polarization of the laser used to drive the source allows the helicity-correlated changes in electron beam parameters to be very small. For example, the electron beam intensity is controlled with an active feedback system which adjusts the light incident on the photocathode, such that the helicity-correlated electron beam intensity variations at the target average to a few ppm in a typical 1 h long run. In addition, the spectrometer is azimuthally symmetric (eight sectors—“octants”), so any small helicity-correlated beam motion effects cancel to lowest order when summing the rate over all the detectors.

As indicated above, a complete description of the neutral weak currents of the nucleon requires measurements at both forward and backward angles. A spectrometer with modest  $\int |\vec{B}| dl$  can be used if one detects the recoil protons for the forward measurement and the scattered electrons for the backward measurement. Further, detection of “forward” protons at about  $70^\circ$  and “backward” electrons at the complementary angle of  $110^\circ$  (in separate measurements) allows for reasonable kinematic leverage to separate the  $G_E^V G_E^Z$  and  $G_M^V G_M^Z$  terms. Thus by reversing the spectrometer with respect to the beam direction, both measurements can be performed with basically the same instrument. Photographs of the experimental setup in the forward and backward configurations are shown in Figs. 2 and 3. A summary of the parameters for the experiment is presented in Table 1. With an

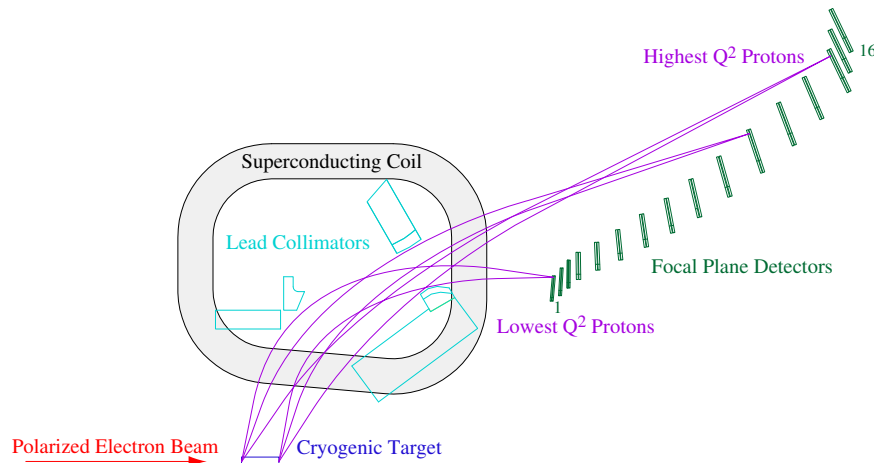


**Fig. 1.** Schematic of some typical trajectories for elastic protons at different  $Q^2$  in the forward measurement. A superconducting coil outline and one octant of collimators, line-of-sight shielding, and focal plane detectors are pictured. Protons of the same  $Q^2$  originating from any location in the target are focused to a common detector. Note that the highest  $Q^2$  protons appear in FPD 14—see text. A photo of the FPDs appears in Fig. 15.

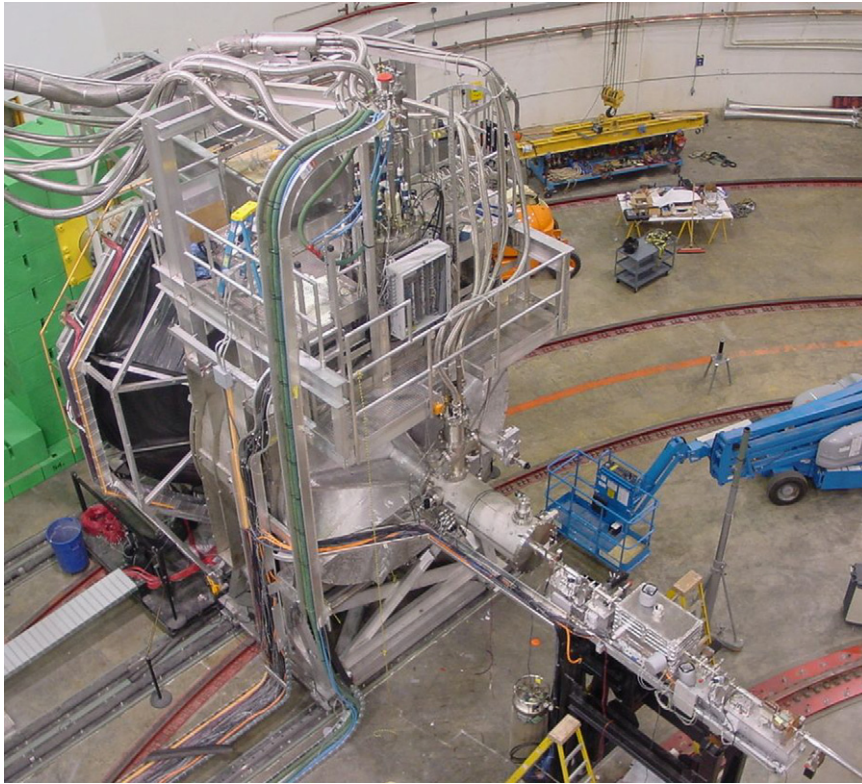


**Fig. 2.** A view of the experimental setup in the forward configuration. The electron beam travels from lower right to upper left. The superconducting magnet is seen just to the left of the center of the frame; the target is centered inside the magnet. Recoil protons from elastic scattering are bent by the magnet to the octants of focal plane detectors (FPDs) whose black covers are visible at left (Octant 7, in the horizontal plane, is the most visible in this image).

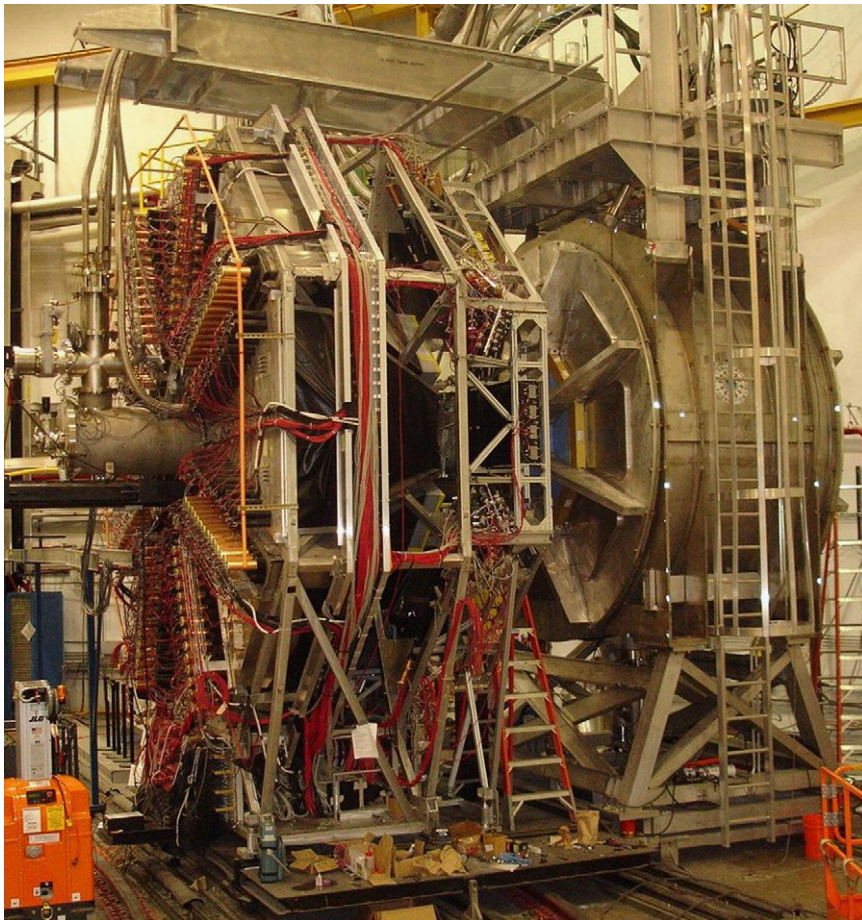


**Fig. 3.** A view of the experimental setup in the backward configuration. The beam enters from the left. The superconducting magnet is on the right of the frame; the target is centered within it. Electrons scattered backward are bent by the magnet into the detector system (shown retracted from its normal position by about 1 m) in the center-left region of the image. The photomultiplier tubes for Octant 3 are closest to the camera at left. Detector supports added for the backward measurement, holding the Cherenkov and cryostat exit detectors (CEDs), are visible just to the right of center.

**Table 1**

Nominal parameters for the forward and backward measurements which illustrate the general capabilities of the G0 apparatus. The scattering angle acceptances are different for forward and backward measurements because of the differing correlation between scattering angle and momentum for the two cases.

Quantity	Forward protons	Backward electrons
Beam energy (GeV)	3.0	0.36, 0.69
Target length (cm)	20	20
Beam current ( $\mu\text{A}$ )	40	20–60
$p$ (GeV/c)	0.35–1.13	0.24, 0.35
$\theta_{\text{elastic}}$ (deg)	52.0–76.5	100–118
$Q^2$ ( $\text{GeV}^2$ )	0.12–1.0	0.22, 0.63
$\Delta\phi$	$0.44 \cdot 2\pi$	$0.44 \cdot 2\pi$
$\Delta\Omega_{\text{elastic}}$ (sr)	1.07	0.82
$\int  \vec{B}  dl$ (T m)	1.6	1.6

acceptance that ranges between roughly  $52^\circ$  and  $77^\circ$  in the forward direction and a beam energy of 3 GeV, the full range of momentum transfers can be measured in a single setting. The corresponding proton momenta vary between about 0.35 and 1.13 GeV/c, and the corresponding scattering angles of the (undetected) electrons range from  $6^\circ$  to  $21^\circ$ . For the same range of momentum transfers, the electron momenta at the backward scattering angle of about  $110^\circ$  are also within this range. However, because  $Q^2$  varies slowly with angle in the backward direction, separate measurements are made to sample the desired range of momentum transfer; beam energies of 359 and 684 MeV gave  $Q^2=0.22$  and  $0.63 \text{ GeV}^2$ , respectively. Background processes are rejected using different methods for the forward and backward measurements, as described below.

## 2.2. Forward angle measurement

The choices of detector and electronics for the experiment are dictated by the relatively high rates in the forward measurement. The superconducting magnet system (SMS) is segmented in octants with corresponding detectors; the detector widths within each octant are chosen to give reasonable resolution in forward momentum transfer as well as to limit the rate to  $\sim 2$  MHz (with about 1/2 coming from elastic protons, 1/2 coming from background inelastic protons and pions). Pairs of plastic scintillators with phototubes at each end are chosen for the detector elements. The basic elastic proton event is defined by a coincidence of the left-right mean-timed signals from two such scintillator elements.

In order to separate elastic protons from background in the forward measurement (without explicitly measuring trajectories), time-of-flight (ToF) measurements are used to determine particle momenta. The combination of spectrometer optics and kinematics leads to a situation where inelastic protons and pions in a given detector have higher momenta than the elastic protons and thus appear at earlier times (see also Fig. 21). In order to be able to measure the roughly 20 ns ToF of the elastic protons, the beam for this experiment has 32 ns between electron bunches (in contrast to the usual 2 ns spacing for each experimental hall) using a 31.1875 MHz pulsed laser to operate the electron source. With this arrangement, pions appear at the detectors about 7 ns after the beam passes through the target; inelastic protons arrive after the pions and before elastic protons. ToF spectra are incremented for every beam pulse with custom time-encoding electronics (see Section 7). Care must be taken with ToF start signals, which are generated by passage of the beam bunch through the target, to ensure, for example, they are not helicity-correlated (see also Section 3).

The optics of the magnet are such that the range of  $Q^2$  for the forward measurement is dispersed along the focal surface. As the recoiling elastic proton angle decreases (and its momentum

increases), the trajectory intersects the focal surface further from the beam axis, as illustrated in Fig. 1. This allows a separation of  $Q^2$  simply by segmenting each octant into a number of separate detector elements. The combination of the rate limit and reasonable  $Q^2$  resolution leads us to 15 detector elements per octant (“focal plane detectors” or FPDs). At the top of the focal surface the proton trajectories “turn around” with higher  $Q^2$  protons starting to again move closer to the beam axis. In the top two detectors, additional  $Q^2$  resolution is obtained by separating the elastic protons by ToF. A 16th detector is used at the very top of the focal surface to help monitor backgrounds.

## 2.3. Backward angle measurement

The backward angle measurements are qualitatively different for two reasons: electrons are detected and the range of  $Q^2$  available in a single setting is small. Because the electrons are ultra-relativistic, ToF cannot be used to separate inelastic and elastic electrons. Therefore, the more traditional approach of trajectory measurement is used for the backward angle measurements. A set of small scintillators is placed near the exit window of the magnet (“cryostat exit detectors” or CEDs) in each octant. Certain combinations of CED and FPD detectors correspond to the correct combination of momentum and angle for the elastic electrons; other combinations correspond to inelastic electrons (see also Fig. 22). For the backward angle measurements, the mean-timed signals from the FPDs<sup>41</sup> are combined with the corresponding signals from the CEDs (using a programmable logic array) to sort the events. As with the FPDs, the phototubes for the CEDs are located in a low magnetic field region using long light guides.

Negative pions pose a different kind of problem for the backward angle measurements, as they cannot be distinguished using the CED–FPD detector pairs described above. An aerogel Cherenkov counter with a threshold pion momentum of about 570 MeV/c, above the range of  $\pi^-$  momenta accepted, is used to eliminate them from the electron trigger. This counter is placed between the CEDs and the FPDs with the phototubes again located in a relatively low field region. The Cherenkov is most important in the measurement with the deuterium target where quasi-free  $\pi^-$  production from neutrons yields  $\pi/e$  ratios of order 100 at the highest momentum transfers. (For the hydrogen target, the  $\pi^-$  are essentially all produced in the aluminum target windows.)

## 2.4. Counting rate effects

Because individual detector events are counted rather than integrated in this experiment (integration is more common in parity-violation measurements because of the high rates [9,10]), rate corrections are important in both the forward (deadtime) and backward angle (deadtime and accidental coincidences) measurements. They are corrected directly from beam current dependence of the trigger rates and from single measurements; helicity-correlated beam current variation effects are corrected together with other helicity-correlated parameters such as beam position (see also Sections 3 and 7).

## 3. Polarized beam

Like all parity-violating electron scattering experiments, the G0 experiment requires a polarized electron beam of high

<sup>41</sup> In order to reduce low-energy backgrounds, the mean-timed signal for a given FPD detector element (consisting of a front/back scintillator pair) is formed by using one tube (at opposite ends) of each of the front and back FPD.

intensity and the ability to control and accurately measure its properties. These requirements are driven by both the statistical and systematic error goals of the experiment. The high figure of merit ( $P^2I$ ) needed to achieve a small statistical error is obtained with a high current ( $I \sim 20\text{--}60 \mu\text{A}$ ) and high polarization ( $P > 70\%$ ) electron beam. The small asymmetries demand that careful attention must be paid to the helicity-correlated properties of the beam. These properties must be measured and controlled well enough so that any correction made to the measured asymmetries is relatively small and well-understood. Achieving these goals requires specialized subsystems and a degree of coordination between the experimental and accelerator operations that are not typical of more conventional electron scattering experiments. In addition to the specialized polarized beam needs typical of parity-violating electron scattering experiments, the forward angle portion of the G0 experiment also requires a time structure different from the usual time structure of the CEBAF accelerator at Jefferson Lab.

### 3.1. Polarized source

The polarized source of the CEBAF accelerator is based on the photoemission from GaAs photocathodes of polarized electrons which are accelerated to 100 kV in an electron “gun”. Detailed descriptions of the polarized source and past performance can be found in Ref. [11]. For the G0 experiment, strained GaAs photocathodes [12] are used. These crystals typically provide electron beam polarizations of  $\sim 70\text{--}85\%$  at the desired currents. The backward angle measurement utilized the so-called superlattice strained cathodes, yielding the polarizations in the 85% range [13]. Laser light from up to three different drive lasers (for the three CEBAF experimental halls) is incident on the photocathode through a vacuum window. The drive lasers emit radio-frequency pulsed light with typically  $\sim 100$  ps pulse widths, synchronous with subharmonics of the CEBAF accelerating frequency of 1497 MHz. The electrode structure of the gun then focuses and accelerates the electrons to a kinetic energy of 100 keV. The standard repetition rate for beam delivered to a single experimental hall from the CEBAF accelerator is 499 MHz [14]; this is the mode used for backward angle G0 running.

To make use of the ToF technique for forward angle running, the G0 experiment requires a lower repetition rate (31.1875 MHz), giving a 32 ns spacing between beam pulses. To maintain high average current at the lower repetition rate, a Time-Bandwidth Products [15] Ti-Sapphire laser providing 300 mW at 840 nm is used. It is important that the random noise in both the intensity and direction of the laser light be small at the helicity-reversal frequency of the experiment. In practice, the r.m.s. spread in beam parameters in the experimental hall, as determined from measurements made at the 30 Hz helicity-reversal frequency, is always  $< 0.1\%$  for intensity and  $< 10 \mu\text{m}$  for the centroid of the beam position.

The other significant injector issue for forward angle running is beam transport. The current requirements ( $40 \mu\text{A}$  at 31 MHz) imply a peak charge of 1.3 pC/micropulse, in comparison to the more typical value of 0.2 pC ( $100 \mu\text{A}$  at 499 MHz) for usual high-current operation. Using standard settings, pulses with this high peak charge suffer significant emittance growth due to space charge effects in the 10 m long 100 keV region, leading to significant transmission losses and poor quality beam. An acceptable solution was achieved with several modifications to the injector region hardware and tuning procedures, including adding new magnets, modifying typical laser parameters, and stabilizing RF systems. A tune was developed that satisfied the requirements of G0 and those of a simultaneously running experiment in Hall A [16] that required a very small fractional energy spread

( $2.5 \times 10^{-5}$ ). Complete details of these developments can be found elsewhere [17].

### 3.2. Beam monitoring and control

For the G0 experiment, it is important to have continuous monitoring of essential beam properties so corrections for helicity-correlated beam properties can be made. When the beam helicity is reversed, ideally, no other property of the beam would change. In reality, many properties of the beam, such as position, angle, and current are observed to change. This causes the false asymmetry

$$A_{\text{false}} = \sum_{i=1}^N \frac{1}{2Y} \frac{\partial Y}{\partial P_i} \Delta P_i \quad (5)$$

where  $Y$  is the number of detected scattering events normalized to beam current, the  $P_i$  are the beam properties (position, angle, current, and energy), and the  $\Delta P_i = P_i^+ - P_i^-$  are the helicity-correlated differences of those beam properties. Generally, these false asymmetries are kept small by careful beam setup or by active feedback as described below. In this section, we discuss beam monitoring and the beam controls necessary for measurement of both the yield slopes ( $\partial Y / \partial P_i$ ) and the correlated differences ( $\Delta P_i$ ).

The beam current is measured with two microwave cavity monitors installed in the Hall C beam line approximately 40 m upstream of the G0 target. The monitors are cylindrical, stainless steel cavities resonant in the  $\text{TM}_{010}$  mode at 1497 MHz and with a  $Q \sim 500$ . Beam electrons passing through the cavity excite a resonance; the energy is extracted from an antenna installed in the cavity. This is a convenient resonant mode for measuring the beam current because the spatial dependence of the electric field amplitude is nearly constant in the center of the cavity, thus making the response relatively insensitive to beam position. The high frequency signal is mixed down to a DC level, which is measured using a voltage-to-frequency converter and a scaler that is read out at the same rate as the rest of the data in the experiment. The intrinsic noise level in the monitors at the 30 Hz helicity-reversal rate is measured (by comparing two nearby monitors) to be  $\sim 40$  ppm (compared to typical beam current fluctuations of 500–1000 ppm).

The beam position is measured at many points along the Hall C beam line with “stripline” beam position monitors [18]. These monitors consist of a set of four thin wires placed symmetrically around the beam; each wire has a length of one quarter wavelength at 1497 MHz. Beam power coupled into the four antennae at 1497 MHz is downconverted to a lower frequency, filtered, and converted to a DC voltage. The monitors are outfitted with switched electrode electronics [19], supplemented with special sample and hold modules to provide a signal for each antenna. The resulting voltage signals are sent through voltage-to-frequency converters and recorded with scalers read out at the same rate as the rest of the data in the experiment. Linear combinations of antenna signals are used to extract the beam positions in software. The electron beam position and angle projected to the target are determined with a pair of stripline monitors separated by 2.5 m with a midpoint 4.8 m upstream of the target. The electron beam energy is determined from the in-plane beam position measured by a similar monitor located at the center of the Hall C arc, where the beam dispersion is 40 mm/%. The intrinsic noise level in these monitors at the 30 Hz helicity-reversal rate is measured (again by comparing two nearby monitors) to be  $3 \mu\text{m}$  (compared to typical beam position fluctuations of  $\sim 10 \mu\text{m}$ ).

Beam “halo” is a generic term for electrons associated with the incident beam that are radially far ( $> 10 \sigma$ ) from the main beam.

Significant beam halo can interact with an 11 mm diameter flange that is part of the G0 target cell. To minimize this interaction our beam specification requires that  $< 1 \times 10^{-6}$  of the electrons in the beam are located outside a 3 mm radius from the center of the beam. The amount of beam halo is continuously monitored using a 2 mm thick aluminum target with a 6 mm diameter hole in it, located 8 m upstream of the G0 target. Scattered particles from beam interactions with this “halo target” are detected at large ( $\sim 15^\circ$ ) and small ( $\sim 3^\circ$ ) angles. The detectors consist of 5 cm photomultiplier tubes attached to small pieces of lucite or scintillator. The system is calibrated by directing a 5 nA beam into the 2 mm thick aluminum frame of the halo target. With the normal beam tune it is possible to achieve the halo specification on a routine basis (corresponding to negligible rates in the G0 spectrometer detectors). The halo monitor is useful as a diagnostic of significant changes in the beam tune that require corrective action.

Measurements of the yield slopes,  $\partial Y/\partial P_i$ , are made by deliberately varying the beam parameters, or by using the natural variations thereof. Beam position and angle at the target are varied periodically using a set of six air-core steering coils positioned downstream of the Hall C dispersive arc. The positions of the coils are chosen to insure the space of  $x$  and  $y$  positions and angles at the target is adequately spanned (typical ranges of  $\pm 0.5$  mm and  $\pm 0.5$  mr, respectively). The beam energy and current are periodically modulated by controlling the power input to an accelerating cavity in the CEBAF accelerator’s South Linac and the beam current using polarized source intensity control (described below), respectively.

### 3.3. Helicity control electronics

The helicity of the electron beam is set by the polarization of laser light incident on the strained GaAs photocathode. The polarization is controlled by a Pockels cell driven by high voltage power supplies set to correspond to  $\pm \lambda/4$  phase retardation, or approximately  $\pm 2.5$  kV at our nominal laser wavelength. A high voltage switch, driven by a digital “helicity signal”, determines which supply drives the Pockels cell. The helicity control electronics, built in a single VME module around a field programmable gate array (FPGA), generates various timing signals, including that for helicity, as shown in Fig. 4.

The macropulse trigger (MPS) signal is the primary data-taking integration gate for the experiment and is set to twice the period of the 60 Hz line power. All signals in the experiment are integrated over this period, allowing for the dominant 60 Hz noise (and that of the highest subharmonic) in the electron beam properties and electronic signals to be averaged out. The MPS “off” state, typically  $500 \mu\text{s}$  ( $T_{\text{wait}}$ ), is set to allow the Pockels cell to stabilize after a helicity change. During this period the experiment takes no data, and all the scalers are read out.

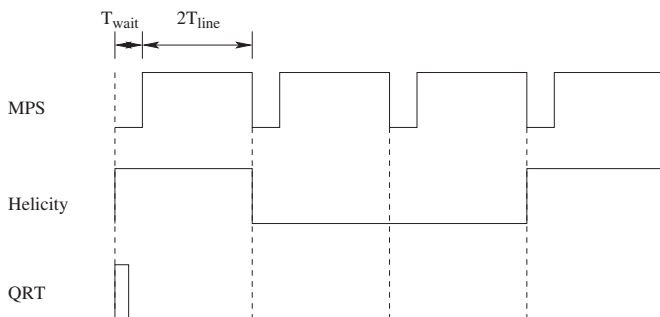


Fig. 4. Timing scheme of the signals from the helicity control electronics.  $T_{\text{line}} = 1/60$  s is the power line period.

The beam helicity is changed relatively rapidly to reduce the effect of slow drifts. To provide exact cancelation of linear drifts in an asymmetry measurement, we generate the helicity signals in a quartet (“QRT”) sequence. The initial helicity state of a sequence is chosen randomly by a pseudorandom number generator programmed into the FPGA. This initial helicity state determines the rest of the QRT sequence,  $+-+ +$  or  $-+ - +$ , and generates a corresponding control signal for the acquisition electronics.

All signals from the helicity control electronics are delivered to the acquisition electronics via fiber optic cable to insure complete ground isolation, and eliminate a possible source of false asymmetries. Other cross-talk between the helicity control electronics and the acquisition electronics is suppressed by delaying the helicity signal reported to the acquisition electronics by eight MPS signals relative to the actual helicity signal sent to the Pockels cell high voltage switch. The true helicity is reconstructed in software from the delayed information and cross-checked with knowledge of the pseudorandom pattern.

### 3.4. Beam position and intensity control

As indicated in Eq. (5), it is very important to minimize the helicity-correlation in beam intensity, position, angle, and energy. This is accomplished by careful setup of both the polarized injector laser beam and the accelerator optics to minimize helicity-correlation, as well as by active feedback to the injector.

One of the most important sources of helicity-correlated intensity and position differences in the electron beam is the Pockels cell that sets the laser helicity. The small residual linear polarization component produced by the cell (different for the two nominal circular polarization states) is transported to the crystal with an efficiency dependent on its orientation. The result is helicity-correlated variations in the laser intensity; a similar effect arising from different steering of the laser beam for the two polarization states is partly responsible for the helicity-correlated position differences. In addition to the interaction with the optical elements, the overall “analyzing power” of the strained GaAs photocathode plays an important role. The photocathode quantum efficiency depends on the orientation of the residual linear polarization [20], and can, in addition, have substantial overall gradients. Depending on the state of the system, this can result in rather substantial intensity asymmetries ( $\sim 10,000$  ppm) and position differences ( $\sim 10,000$  nm).

The setup of the accelerator system to achieve small helicity-correlations in beam properties involves three main elements. First, a rotatable  $\lambda/2$  waveplate is inserted into the laser line just downstream of the helicity Pockels cell [21] to rotate the residual linear component to minimize the intensity asymmetry and position differences. Second, care is taken in the accelerator tuning to realize the natural “adiabatic damping” in the acceleration process. For an ideally tuned accelerator, the transverse position variations of the beam are reduced  $\propto 1/\sqrt{p}$  where  $p$  is the beam momentum. Due to imperfections in the electron beam transport, the full suppression is never achieved, but suppression factors of 10–25 are observed between position differences in the experimental hall versus those in the injector region. After these two passive measures, the intensity asymmetries observed at the target are typically  $< 100$  ppm, while the position differences are typically  $< 300$  nm. In both the forward and backward angle measurements, active feedback is used to improve the intensity asymmetries. For the backward angle measurements, it is found that more careful alignment of the optical elements (especially that of the helicity Pockels cell) could reduce the position differences to  $\sim 20$  nm; for the forward angle measurements, position differences are reduced by active feedback. Intensity asymmetries are reduced with feedback to the IA (intensity

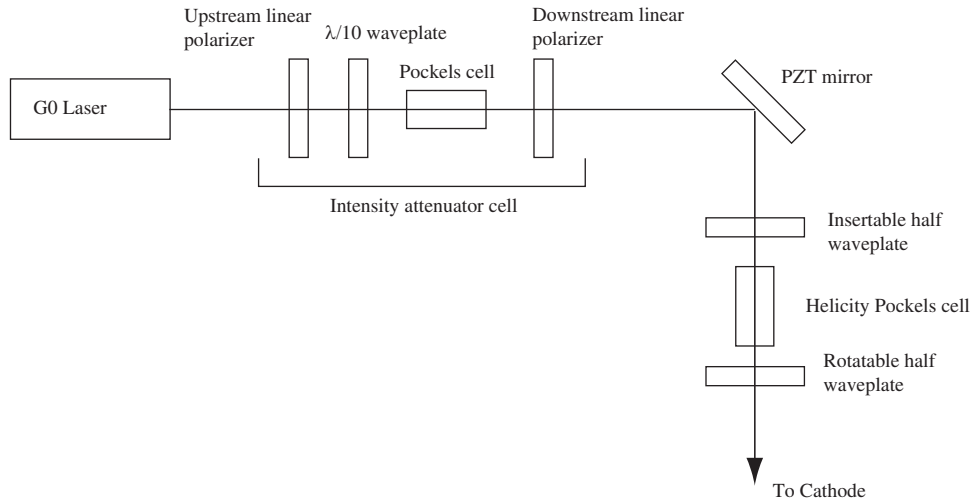


Fig. 5. A schematic illustration of the important devices associated with the minimization of helicity-correlated effects in the beam current and position.

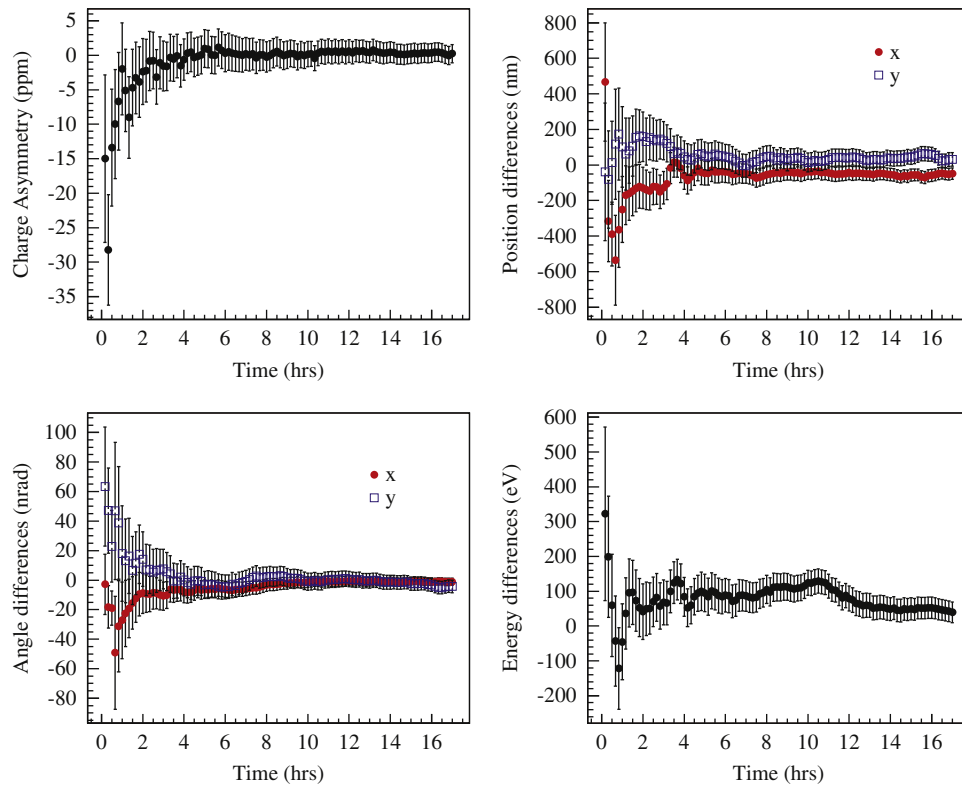


Fig. 6. Feedback results (forward angle) with both the charge and position feedback circuits operating. The cumulative averages of the charge asymmetry (upper left), horizontal and vertical position differences (upper right), horizontal and vertical angle differences (lower left) and energy differences (lower right) are plotted versus time from the start of a feedback cycle. As these are running averages, successive data points are highly correlated.

attenuator) cell (Fig. 5). It consists of two linear polarizers oriented parallel to each other with a Pockels cell in between. The Pockels cell is operated at low, helicity-dependent voltages (0–50 V) to change the transmission of the attenuator.<sup>42</sup> During regular running, the intensity asymmetry is measured for 3 min (during which time it is typically measured with a precision of 10–20 ppm) and then corrected in an automated cycle (see Fig. 6).

<sup>42</sup> The  $\lambda/10$  waveplate is necessary to insure a non-zero slope in the intensity versus voltage relationship when the Pockels cell is operating at low voltage.

Helicity-correlated beam position differences are corrected during forward angle running by feeding back to a piezoelectric-controlled steering mirror which moves the laser beam on the photocathode in a helicity-correlated manner (Fig. 5). In this case, the beam position differences are measured and corrected on a 30 min cycle (using measurements with a precision of 100–200 nm, see Fig. 6). In practice, it is found that these intensity and beam position ( $x$  and  $y$ ) controls are not completely orthogonal; a full  $3 \times 3$  matrix system is required for successful feedback [22,23].

Lastly, Fig. 5 also shows the insertable half-wave plate (IHP) used to reverse the sense of the beam helicity relative to all electronic signals in the polarized source (the half-wave plate

changes right-circular polarization to left-, and vice versa). The measured asymmetries reverse as expected with the IHWP “OUT” to “IN” (helicity reversed) changes as illustrated in Figs. 7 and 8, showing no indication of contributions from electronic cross-talk. The asymmetry for FPD 9 (forward angle) is shown in the first figure for the 23 separate data-taking periods with different IHWP positions demonstrating good statistical consistency. The overall consistency and reversal dependence for four different ToF regions (forward angle) is shown in the IN+OUT summed asymmetries in Fig. 8.

### 3.5. Polarimetry

The electron beam polarization is measured periodically using the Hall C Møller polarimeterA [24]. The polarimeter measures

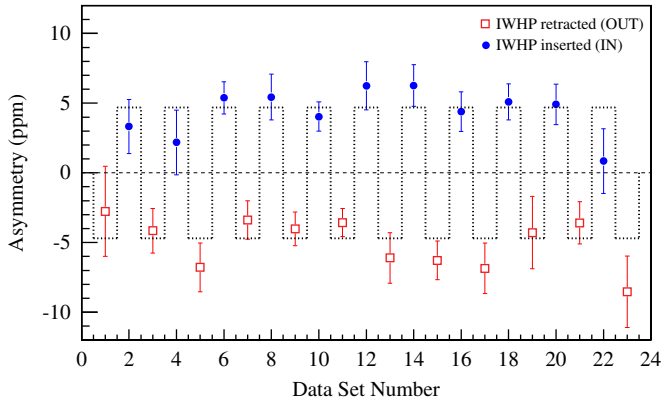


**Fig. 7.** Asymmetries of forward angle elastic protons in FPD 9. The squares (circles) correspond to the data with the insertable half-wave plate retracted (inserted). The measurements correspond to an average asymmetry of  $-4.72 \pm 0.32$  ppm ( $\chi^2/d.o.f. = 18.0/22$ ), shown in the figure as the dotted line (with the appropriate changes of sign).

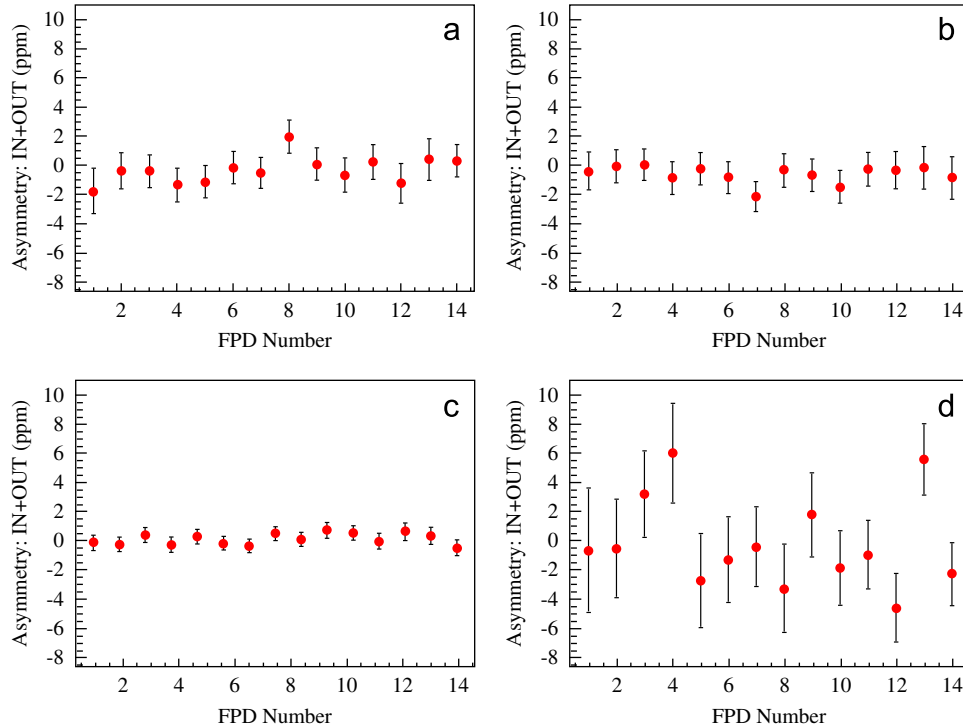


**Fig. 8.** Sum of the forward angle asymmetries with the IHWP inserted (IN) and retracted (OUT) for each FPD; (a) and (b) for ToF windows immediately preceding the elastic window, (c) elastic window and (d) window following the elastic window. The average asymmetry (ppm) and  $\chi^2/\nu$  are:  $-0.28 \pm 0.31, 0.58$ ;  $-0.64 \pm 0.31, 0.29$ ;  $0.02 \pm 0.12, 0.65$ ; and  $-0.45 \pm 0.74, 1.34$ , for (a), (b), (c) and (d), respectively. The widths of the time windows for (a) and (b) are half that of the elastic window; window (d) has the same width as that of the elastic.

the asymmetry in the cross-section for electron–electron scattering, for which the analyzing power is accurately known. The target electrons are provided by a pure iron foil saturated in a 3 T field. The scattered and recoiling Møller electrons produced at  $90^\circ$  in the center of mass are detected in coincidence using a symmetric apparatus. The beam polarization is typically measured with  $< 1\%$  statistical error in 5 min. For the forward angle data-taking, the average beam polarization over the entire data set is measured to be  $73.7 \pm 1.0\%$  where the uncertainty is dominated by the systematic uncertainty in extrapolation from the low beam current of the polarization measurement to the operating current of the main data-taking [25]. The polarization for the backward angle experiment is  $85.8 \pm 2.1$  (1.4)% at 359 MeV (684 MeV), again dominated by systematic uncertainties. For the higher energy, in addition to the beam current extrapolation uncertainty, there is an additional contribution of comparable size due to beam tuning effects. For the low-energy running, the Møller polarimeter could not be operated; instead a 5 MeV Mott polarimeter in the injector region, calibrated using the Møller measurement at 684 MeV (and incorporating knowledge of the beam spin transport [26]), is used to monitor the polarization [27]. The uncertainty in this calibration is the origin of the additional factor in the overall low-energy polarization uncertainty.

### 3.6. Raster

The intrinsic diameter of the electron beam ( $\sim 200 \mu\text{m}$ ) is such that at the currents used in these measurements, 20–60  $\mu\text{A}$ , the power density on the cryogenic target would be  $\sim 1 \text{ kW}/\text{mm}^2$ . To reduce this power density, and therefore the magnitude of beam-induced density fluctuations in the target (see Section 4.4), the beam is rastered using two magnets located approximately 20 m upstream of the target. The fast raster system [28] generates a

square,  $\sim 2 \times 2 \text{ mm}^2$  pattern by sweeping the fields in  $x, y$  with triangular waveforms of 24.96 and 25.08 kHz frequency, respectively, yielding a pattern with 95% uniformity in the beam density.

#### 4. Target system

The target system consists of the main cryogenic target, filled with either liquid hydrogen or liquid deuterium, as well as auxiliary solid targets for diagnostic purposes. In order to determine the backgrounds from the aluminum target cell, the main cryogenic target could also be operated with gas at a temperature several degrees above that used for liquid operation. The auxiliary solid targets are C and Al; a “halo” target (actually just a 5.6 mm diameter hole—distinct from the upstream halo monitor target—see Section 3.2) is also included. Finally, as discussed below, an additional thin aluminum target could be placed in the beam just downstream of the cryogenic cell to better characterize the downstream window of the cell (see Fig. 9).

##### 4.1. Cryogenic target

The G0 cryogenic target is a closed-loop recirculating system for liquid hydrogen and deuterium, with a 20 cm long target cell that resides inside the vacuum enclosure of the superconducting magnet. Here we provide an overview of the target and its performance; a more detailed description is available elsewhere [7,31].

Design considerations for the target include the beam power requirements ( $\sim 340 \text{ W}$  at  $60 \mu\text{A}$  beam current), space constraints due to the 60 cm diameter opening in the magnet, non-magnetic construction for the parts in the magnetic field, and the need for reliable operation for many months of operation with no servicing. As a result, the cryogenic loop is oriented horizontally.

The target fluid is circulated with a velocity  $\sim \text{m/s}$  through the cryogenic loop in order to dissipate the power deposited by the electron beam as it passes through the target cell. The fluid is

pumped by a Barber Nichols [32] custom DC brushless, “sensorless” motor, driven by a sensorless controller. A tachometer, consisting of a Cu coil and a small permanent magnet, measures the pump rotation frequency. The variable voltage induced by the changing magnetic flux through the Cu coil as the motor shaft rotates is monitored by a digital multimeter enabled in frequency mode. The nominal operating frequency of the motor is 30 Hz; the maximum available torque in liquid hydrogen is found to be 0.16 N m at 42.7 Hz.

On the opposite side of the cryogenic loop is a counterflow heat exchanger with finned Cu tubing on the target fluid side. The coolant side uses helium gas at 15 K and 12 atm from the Jefferson Lab End Station Refrigerator (ESR). The effective area for heat exchange is  $9501 \text{ cm}^2$  on the target side and  $1110 \text{ cm}^2$  on the coolant side, with a measured heat transfer coefficient of  $214 \text{ W/K}$  under normal operating conditions. Tests of the maximum performance of the heat exchanger found it capable of removing up to  $1000 \text{ W}$  of heat from the liquid hydrogen at its nominal operating point (19 K and 1.7 atm) when using 80% of the available coolant from the ESR.

After passing through the heat exchanger, the target fluid enters a target manifold to which the thin-walled target cell is soldered. It holds both the primary hydrogen cell and a secondary cell filled with helium that serves as the entrance window to the hydrogen system. The primary cell is a thin-walled cylinder machined from one piece of Al-7075, of length 23 cm and inner diameter 5 cm. An exit window spot, centered on the beam axis, is machined to a thickness 0.076 mm and diameter 8 mm; the remainder of the shell is approximately 0.178 mm thick. Target cells are pressure tested to 590 kPa. The target fluid is directed longitudinally down the center of the target cell by a thin-walled inner cone. Small holes in the side of the cone produce turbulence and allow for mixing in the longitudinal flow. The 16 cm long helium cell ( $\sim 0.07 \text{ g/cm}^2$ ) upstream of the primary cell is attached to the manifold with a flange and indium seal. The downstream window of the helium cell, soldered to the main body, is 0.228 mm thick and serves as the entrance window to the hydrogen. To reduce variations in target length for differing beam

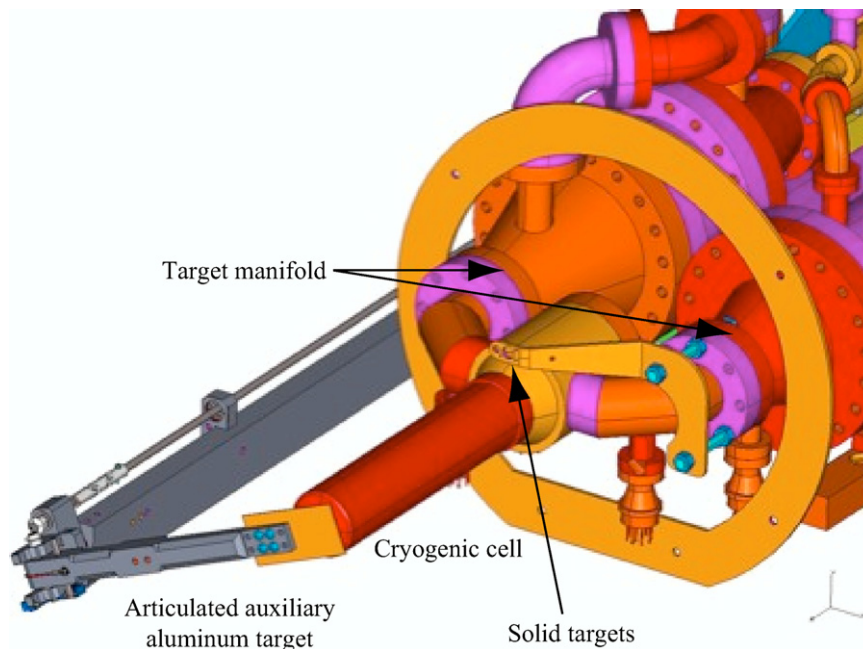


**Fig. 9.** Drawing of the cryogenic target, with solid target frame shown above the cylindrical cryogenic cell, and with the auxiliary articulated aluminum target downstream of the cell shown in the inserted position. The horizontal manifold contains the pump (left) and the heat exchanger (right). The beam enters from the upper right along the axis of the cryogenic cell.

positions, the radius of curvature of this window is matched to that of the primary exit window; the helium cell is maintained at the same pressure and temperature as the hydrogen cell. At its upstream end, the helium cell has a 0.178 mm thick Al window. The length of liquid hydrogen seen by the detector system is 20 cm or 1.44 g/cm<sup>2</sup> at the operating conditions of 19 K and 170 kPa; the net material in the three windows seen by the detector is 0.130 g/cm<sup>2</sup>. In addition, for studies of backgrounds arising from these entrance and exit windows, the cryotarget is also successfully operated with hydrogen gas at 220 kPa pressure at two operating temperatures, 28 and 33 K.

The cryogenic loop is supported inside the SMS vacuum system on a cantilevered platform connected to a service module upstream of the SMS. The cantilever and service module are designed and constructed by Thermionics [33]. The location of the target with respect to the incident beam is controlled by four actuators (two vertical, two horizontal) which provide pitch, yaw, and translation of the entire cryogenic target loop vertically and horizontally. The target is aligned to the magnet-beam axis to < 1 mm horizontally and vertically.

The control system for the cryogenic target has the primary functions of monitoring and periodically recording the various target parameters, providing warnings of critical conditions, and, using a proportional-integral-differential (PID) feedback system, maintaining the target fluid at a constant temperature. It is based on a VME processor, standard I/O modules, and the EPICS [29] slow controls system. The temperature of the target fluid is monitored in six locations within the cryogenic loop with Lakeshore Cernox CX-1070-AA [34] resistors immersed directly in the fluid. Two additional sensors monitor the temperature of the helium coolant at each end of the heat exchanger. Target pressure is monitored in the gas system. Pressure excursions in the target loop are minimized by a 9450 l ballast tank coupled to the gas-handling system. The temperature of the target is maintained with a resistive heater located just downstream of the target manifold before the target fluid enters the circulating pump. The heater is constructed of three coils of Ni–Cr alloy ribbon, each with a resistance of 3.5 Ω, wired in parallel, and driven by a 40 V, 25 A DC power supply. During normal operations, the total heat load on the target is held constant at approximately 400 W, coming from either the incident beam or from the heater. The feedback system tracks the beam current incident on the target, subtracts the deposited beam power from the target power, and sets the current on the heater to make up the deficit. Temperature excursions, even after a beam trip, are less than 0.2 K.

#### 4.2. Solid targets

In addition to the cryogenic loop, several solid targets are mounted on the target manifold to allow measurement of background processes. For example, events from the aluminum target windows typically account for a few % of the elastic yield in the forward angle measurement, and up to 10–15% in the backward angle measurement.

Using the position actuators, the target assembly can be pitched downwards for an out-of-beam, no-target geometry. A dummy target frame is situated between these two positions, and consists of a 3.2 mm thick aluminum frame bolted to the cryogenic target manifold flange. This frame, 13.4 cm upstream of the center of the 20 cm long cryogenic cell, supports three different targets just above the cryogenic cell, insuring there is no interference with the trajectory of the protons or electrons scattered anywhere along the 20 cm length of the main cryogenic target. The three targets are: a 5 mm thick carbon target mounted over a 10 mm diameter hole, a bare 5.6 mm hole used to characterize

the beam halo, and a third target which simply consists of a surveyed spot on the aluminum frame itself.

An auxiliary aluminum target is provided 1 cm downstream of the exit window of the cryogenic cell and is used to characterize the response from the downstream target window; see Fig. 9. This 0.76 mm thick Al foil can be articulated on or off the beam axis independently of the other targets. It is used in conjunction with a special 0.085 mm thick tungsten foil target 48 cm upstream of the aluminum foil target. The tungsten target is the same thickness (in radiation lengths) as the cryogenic target, but is located well upstream of the detector acceptance. It is used to radiate photons for Al foil target measurements, mimicking the background at the exit window from photons produced within the cryogenic target.

#### 4.3. Luminosity monitors

Primarily to study and monitor beam-induced variations in fluid density in the target, a set of luminosity monitors is located downstream of the target at very forward angles [30]. Short-term target density fluctuations can contribute to the overall statistical noise in the measurement, combining with that from the particle counting statistics. The experimental goal is to reduce the target density effects on the noise to a negligible level by adjusting the operating parameters of the beam (size) and target (flow speed, etc.).

The luminosity detectors consist of synthetic quartz Cherenkov cubes coupled to low-gain photomultiplier tubes (PMT) at an angle of approximately 2° with respect to the incident beam. A total of eight detectors are placed symmetrically about the beam line. Due to the very high rate of electrons coming primarily from Møller scattering in the target, the phototube current is integrated over the 30 Hz helicity window. It is then converted to a voltage, passed through a voltage-to-frequency converter, and counted with scalars. These electronics are similar to those used for the beam position and current monitors described in Section 3.2. The luminosity monitors provide a significantly higher precision for small changes in asymmetry widths, each having an intrinsic width of 200 ppm per QRT with a 40 μA beam current. This is compared to the asymmetry width of each of the 15 rings of G0 FPD detectors of approximately 1200 ppm in the forward measurement and a minimum of 5000 ppm for the full elastic signal at backward angles. However, because the luminosity monitors are more sensitive to other small systematic effects such as small changes in beam halo or scraping of the beam upstream of the target, some care must be taken to separate effects in determining the target density contributions to detector signal widths.

#### 4.4. Target performance

Prior to operation with liquid hydrogen, tests of the target system were carried out with cold helium gas in order to establish the performance characteristics of the heat exchanger, and with liquid neon in order to assess the safety of the gas handling system in the event of a catastrophic failure [31].

Tests with liquid hydrogen included assessment of density fluctuations via measurement of the width of asymmetry distributions as a function of beam current, target pump speed, beam raster size [28] and intrinsic beam spot size. For the initial, forward angle measurement, in order to improve the sensitivity of these tests relative to the statistical precision of a single G0 detector, groups of detectors were averaged together and integrated over ToF. In addition, the asymmetry distributions for the luminosity monitors (Section 4.3) provided additional information.

A detailed discussion of these tests and analysis of the data can be found in Ref. [7]. The overall conclusion is, for nominal running conditions with a 40  $\mu\text{A}$  incident beam rastered over a square of side 2 mm, and with the target circulating pump operating at approximately 30 Hz, the maximum contribution to the asymmetry widths coming from density fluctuations (hydrogen or deuterium) is of order  $240 \pm 70$  ppm. This results in at most a 2% increase in the signal width for any  $Q^2$  bin in the forward angle measurement and has a negligible impact in the backward angle measurements. Global density reductions of the liquid due to beam heating were also investigated, and are found to be less than of 1.5% at the nominal operating conditions.

## 5. Magnetic spectrometer

The G0 experiment employs a superconducting magnetic spectrometer (SMS) to analyze the momentum of scattered particles (protons in the forward mode, electrons in the backward mode), to define the angular acceptance for scattered particles, and to provide both magnetic and bulk material shielding for the detectors against backgrounds originating from the target. By reversing the orientation of the spectrometer with respect to the target center, while also reversing the magnet polarity, both the forward proton and backward electron modes are accommodated. The additional conditions placed on the spectrometer magnet by the requirements of the experiment are summarized in Table 2.

### 5.1. Optics

Various optical designs of the SMS were considered, including solenoidal and various dipole/multipole configurations, but it soon became clear that a toroidal spectrometer offered many advantages. The large acceptance arising from a relatively unobstructed geometry, and the intrinsic axial symmetry of a toroid are particularly attractive. In addition, there need be no iron return yokes or pole faces, potential sources of spin-dependent re-scattering, which could produce false asymmetries. The magnetic field of a toroid is negligible near the axis where the target is located, hence beam steering and target polarization effects are minimized. A toroidal magnet can also accommodate both the forward proton and backward electron measurements with a simple reversal of orientation along its axis and a corresponding reversal of the magnet polarity.

The forward-proton measurements place the most restrictive constraints on the spectrometer and therefore drive a number of the design parameters. The size and scale of the spectrometer is set by the larger proton momentum, and the minimum bend angle,  $\alpha$ , of about  $35^\circ$ , is dictated by the requirement that the detectors in their optimal location be shielded from direct view of the target. The goal for the momentum transfer range of the experiment is  $0.1 \leq Q^2 \leq 1.0 \text{ GeV}^2$ . Resolution in  $Q^2$  of order 10% provides a number of distinct measurements in this range. This corresponds, for example, to a momentum resolution,  $\Delta p/p$ , of

about  $\pm 5\%$  at  $Q^2 = 0.5 \text{ GeV}^2$ . In the backward case, it is only necessary to resolve elastic and inelastic electrons, which requires a resolution  $\Delta p/p \geq \pm 10\%$  over the  $Q^2$  range of the experiment.

Although they provide, at best, a crude representation, first-order TRANSPORT [35] matrix elements (detectorcoordinate|targetcoordinate), are useful in discussing the broad characteristics of the SMS. Relative to a central trajectory, the characteristic coordinate pairs are  $x, \theta$  corresponding to the dispersive direction ( $\vec{v} \times \vec{B}$ ) and the scattering angle, and  $y, \phi$  corresponding to the azimuthal coordinates. Because of both relatively better momentum resolution for an extended target, and a smaller detector package (bending toward the axis), “zero-magnification”,  $(x|x) = 0$ , optics is chosen over the usual, focusing,  $(x|\theta) = 0$ , optics. In the  $(x|x) = 0$  case, each point on the focal surface ideally corresponds to a particular  $(p, \theta)$  pair. For the two-body final state in elastic scattering, the correlation between  $p$  and  $\theta$  leads, in principle, to different values of  $Q^2$  for each value of  $x$  at the focal surface. This situation is approximately realized for the forward scattered protons where the momenta vary rapidly with scattering angle. For the backward scattered electrons, deviations from  $(x|x) = 0$  away from the octant median plane dominate the effect from the relatively much smaller variation of momentum with scattering angle.

Operating cost projections dictate that the magnet be superconducting. Construction costs are reduced by using a common cryostat for all the coils. The choice of superconducting technology allows a relatively higher number of ampere-turns near the beam axis, both decreasing the azimuthal obstruction of the coil and allowing the rotation of the inner “edge” of the magnetic field (effected by the taper of the otherwise  $\sim$  rectangular coils at the inside radius as shown in Fig. 10) to move the focal surface outside the cryostat. Eight coils are chosen as a reasonable compromise between azimuthal acceptance and optical aberrations away from the median planes (caused by the stronger curvature of the magnetic field lines near the coils).

Schematic views of the coil outline and cross-section are shown in Fig. 10. A conservative current density of  $5 \text{ kA/cm}^2$  is chosen for the surplus Superconducting Super Collider superconducting wire used. The parameters  $h, w, r, R, A, B$ , and  $\delta$  defined in Fig. 10 are varied to essentially achieve the best zero-magnification condition with the largest solid angle acceptance, subject to a maximum cryostat diameter of 4 m (the size of the door opening in Jefferson Lab Hall C) and the constraint that the focal surface lie outside the cryostat. The optimized values of these parameters are shown in Table 3 along with the central target position and the total coil current ( $5 \text{ kA} \times 144$  turns).

In order to eliminate background and to ensure that the resolution requirements are met, collimators are introduced to define the acceptance. In order to limit the effect of aberrations near the edges of the octants, azimuthal collimators (10 cm thick lead along the trajectory) are used to limit the  $\phi$  acceptance to about  $\pm 10^\circ$ .

“Primary” lead collimators, located at a neck in the envelope of particle trajectories (see Figs. 1 and 11), limit, limit the acceptance in

**Table 2**  
General requirements and design implications for the G0 spectrometer.

Requirement	Strategy	Implications
High statistics	High luminosity High rates	Extended target (20 cm length) Minimal particle tracking
Large $Q^2$ range (forward measurement)	Large $\phi$ acceptance Modest $Q^2$ resolution	Minimal obstruction $1\% \leq \Delta Q^2/Q^2 \leq 10\%$
Low backgrounds	Reduce target background	Line-of-sight shielding (sets minimum bend angle, $\alpha$ )
Low systematics	Axial symmetry Minimize spin-dependent re-scattering	Symmetric spectrometer Iron-free environment, low target field

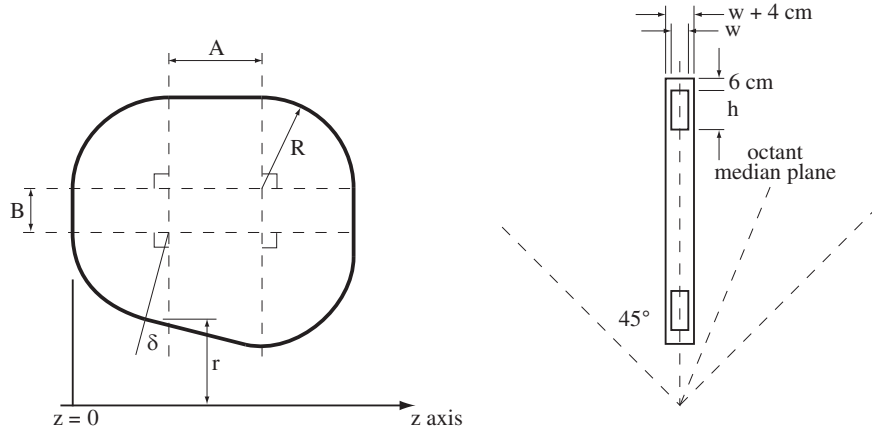


Fig. 10. SMS coil schematic (outside dimensions). Optimized dimensions are listed in Table 3.

**Table 3**  
Optimized G0 spectrometer current distribution parameters (see text).

Quantity	Value
<i>h</i>	18cm
<i>w</i>	8cm
<i>r</i>	42cm
<i>R</i>	50cm
<i>A</i>	65cm
<i>B</i>	28cm
$\delta$	5°
<i>z</i> (target)	44cm
<i>I</i> <sub>coil</sub>	0.72MA

the dispersion direction. Both the low and high momentum limits for elastic protons are defined by the primary collimator nearest the beam line. This lower primary collimator is about 70 cm thick along the line-of-sight from the target to the detectors in order to scatter neutrons effectively. The other two pieces of the primary collimators shown in Fig. 11 reduce background from particles outside the desired acceptance as well as from showering of electrons and photons generated in the target.

For the backward measurements, the momentum resolution of the spectrometer must be sufficient to separate elastic from threshold-inelastic scattering. The leading terms in momentum resolution are

$$\left(\frac{\Delta P}{P}\right)^2 = \left(\frac{x|x}{x|\delta}\right)^2 \cdot \Delta x^2 + \left(\frac{x|\theta}{x|\delta}\right)^2 \cdot \Delta \theta^2. \quad (6)$$

Although the resolution could be improved by reducing the length of the target,  $\Delta x$ , the required resolution is more readily achieved by restricting the angular acceptance  $\Delta \theta$  because of the size of the coefficients in Eq. (6). This restriction is effected by inserting a new set of plastic scintillators (CEDs) near the exit of the magnet cryostat. The combination of the FPDs and CEDs are sufficient to separate elastic and inelastically scattered electrons, and allow us to measure both parity-violating asymmetries simultaneously [36].

### 5.2. Physical design

The collaboration’s reference conceptual design was developed by the primary contractor for magnet fabrication, BWX Technology, Inc. (BWXT) [37]. The magnet was constructed over a period

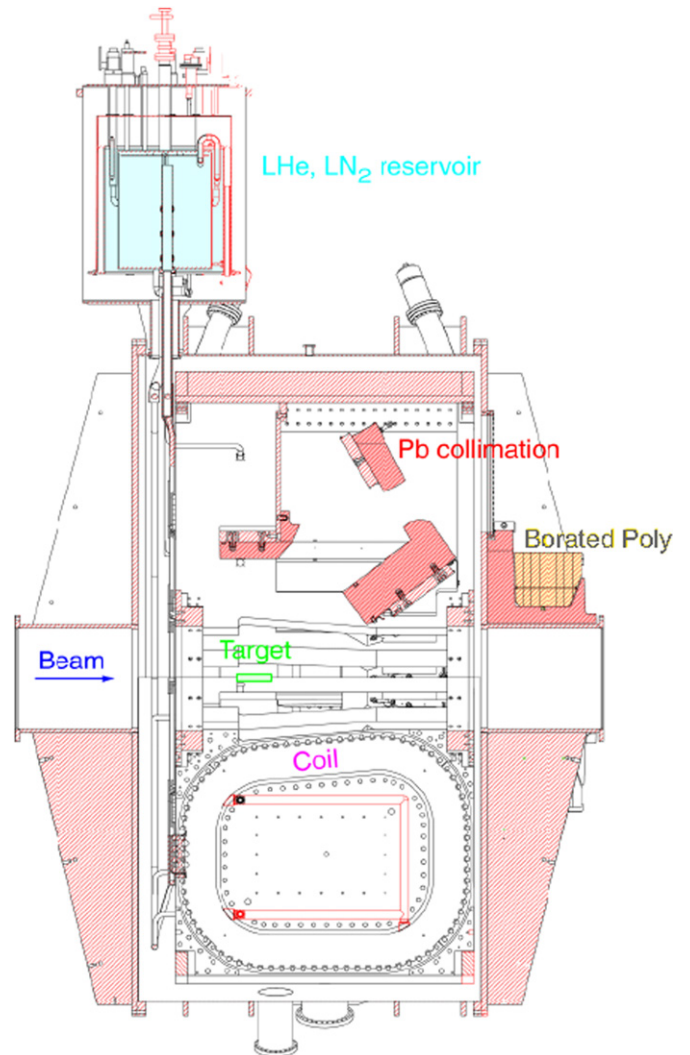


Fig. 11. Cut-away view of the interior of the G0 SMS, showing the placement of the target, magnet coils, collimators and shielding, and the LHe and LN2 reservoirs. In the upper half only the collimation is shown and in the lower half only (a section through) the magnet coil is depicted. The lead collimators are supported within a pie-shaped box as discussed in the text. The U-shaped coil cooling channel is shown within the coil bobbin (outlined by the double lines on the inside of the overall coil package).

of 3.5 years at the facilities of BWXT in Lynchburg, Virginia. Control system development and the initial cooldown were then carried out at the University of Illinois beginning in 2001. The magnet was shipped early to Jefferson Lab in 2002 for installation in Hall C. In Fig. 11, a vertical cross-section along the beam line shows some of the principal parts of the spectrometer which will be discussed in more detail below (see also Ref. [38]).

### 5.2.1. Mechanical design

The G0 spectrometer magnet is made up of eight superconducting coils configured radially around a central bore region. The coils are wound from NbTi superconducting wires in a Rutherford cable configuration, soldered into a copper substrate as shown in Fig. 12. The coils are “dry wound” (i.e., not “potted” with resin) on aluminum coil forms or bobbins in two “double pancake” windings with each layer in a pancake containing 36 turns, yielding 144 turns total. The two double pancakes of a coil are spliced together by overlapping and soldering the adjacent leads. Two layers of 0.25 mm G-10 sheet insulate the pancakes from each other, from the bobbin, and from the coil case. Each coil is contained in an aluminum case which provides conductive cooling from the central bobbin and a mechanism for pre-loading the coils. The Lorentz force between windings of the coils tends to separate adjacent turns leading to reduced thermal contact and potentially to movement which can release sufficient energy to quench the superconductor. To counter these forces and to reduce thermal resistance, the coil windings are clamped and pre-loaded using pairs of jack-bolts mounted in blocks attached

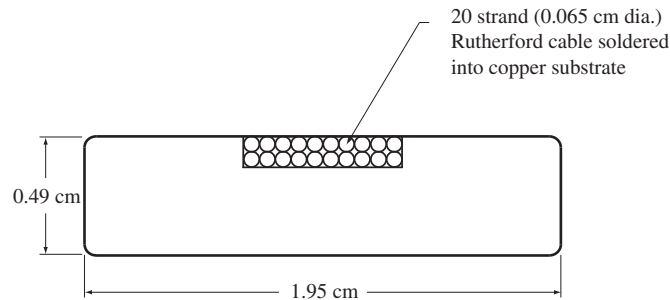


Fig. 12. Cross-section of superconducting cable.

to the coil side plates. Typically the pre-load is 12 kN/cm of coil perimeter.

The conductor is cooled to its operating temperature of 4.5 K by conduction to the central bobbin. The bobbin, in turn, is cooled by liquid helium (LHe) passing through an interior U-shaped channel (see Fig. 11). Four parallel cooling circuits, each consisting of two coils and interconnecting plumbing are fed LHe at the lowest point in each circuit via a supply manifold from a reservoir at the top of the magnet. Each circuit is arranged so that the vertical component of flow is always upward, as shown in Fig. 13. As the LHe flowing through the coils absorbs heat, some boiling occurs, decreasing the bulk density of the fluid. Density differences between the column of LHe in the supply manifold and the lower density two-phase fluid in the coils causes the two-phase fluid to rise, carrying the vapor back to the LHe reservoir. In the reservoir, the evaporating gas is returned to the Jefferson Lab ESR, while liquid is recirculated through supply manifold to the coils.

The eight coils of the spectrometer magnet are bolted to two aluminum, load-bearing hubs at their up-stream and down-stream ends. The aluminum hubs are designed to react against the 52 tonne net inward Lorentz force generated by each coil. The coils are attached to each other on their outer perimeter by up-stream and down-stream octagonal aluminum rings. The allowed coil positioning uncertainty of  $\pm 2$  mm is sufficient to reduce the force between coils due to misalignment away from symmetry to negligible levels.

In order to implement the shielding and collimation discussed in Section 5.1, a collimator module, containing all the shielding internal to the cryostat for a single octant, is hung from the straight sections of the octagonal rings between each pair of adjacent coils (see Fig. 11). Each module is a roughly pie-shaped box made of bolted and welded aluminum. Cast lead alloy blocks are fastened to, or suspended between, the two sides of the box which parallel the coils. A Pb/Ca/Sn/Al alloy [39] is chosen both because of its mechanical hardness and because it has a lower critical field than pure lead. Differential thermal contraction during cooldown between the aluminum structure and lead is significant. To ensure the contraction takes place in a predictable and reproducible way, the lead is installed using a “spring-beam” fastening scheme. Each block of lead is only bolted to a single plate of the aluminum structure and fully constrained at only a single point. Any additional fasteners are mounted to spring

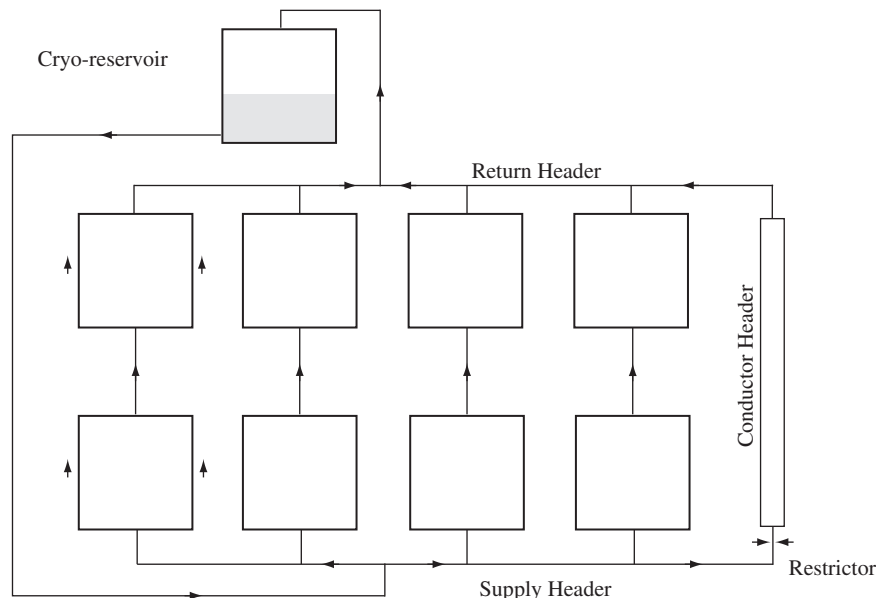


Fig. 13. Liquid helium thermal siphon circuit for SMS cooling.

beams, machined out of the aluminum plate, which could flex and therefore allow relative motion in a less critical direction but not perpendicular to it.

The cold mass, consisting of the coils, collimator modules, and aluminum support structure, and with a weight of 30 tonne, is suspended from the top of the vacuum vessel with four angled tension rods fastened to the octagon rings at the upper corners. The 2.36 cm diameter, 68 cm long rods, made of Inconel 718 for high strength and low thermal conductivity, are equipped with ball joints at both ends and a mechanism for fine length-adjustment at the warm end. The cold mass must be restrained axially and laterally, but allowed to move vertically during cooldown; this constraint is provided by a 3.81 cm diameter, 316 stainless steel “shear pin”, which is bolted to the center of the bottom collimator module. As the cold mass contracts vertically upward during cooldown, the pin slides in a G-10 bushing fixed to the vacuum vessel.

Heat due to radiation and conduction is intercepted using a single liquid nitrogen (LN<sub>2</sub>) shield which surrounds the entire cold mass including the central bore (for radiation entering from the beam line). Thermal siphon flow is used to circulate LN<sub>2</sub> from the reservoir at the top of the cryostat through cooling tubes clamped to the outside cylindrical surface of the shield. The shield end-caps and the central bore tube are cooled by conduction through the aluminum support structure from the outer cylinder. Cut-outs in the central tube, aligned with the apertures between coils, permit scattered particles to pass from the target into the magnetic field. No such provision for particles exiting the magnet is made as multiple scattering at that point in the particle trajectory has a small effect on the position at the detectors. The exterior of the shield, as well as the interior of both ends of the shield, are covered with 20 layers of multi-layer insulation (MLI).

The cold mass and shield are contained in a single vacuum vessel consisting of a 4 m diameter, 2 m long cylindrical shell and two end-caps. The shell is fabricated from 1 cm thick low-permeability ( $\mu < 1.02$ ) stainless steel reinforced with four 2.5 cm thick stiffening ribs and two 5 cm thick end flanges (see Fig. 11). Additional flanged radial penetrations in the cylindrical shell provide ports for the cold-to-warm supports, instrumentation feedthroughs, pressure relief safety valves, and vacuum pumps. Due to the sensitivity of the magnetic verification scheme (see Section 5.3) the end-caps are each fabricated from a circular plate of 3.8 cm thick 6061-T651 aluminum stiffened against deflection by eight roughly triangular 7.6 cm thick ribs connecting the circular plate to a 60 cm inner diameter central beam pipe. The end-caps are bolted to the flanges on the ends of the cylindrical part of the vessel with o-ring seals. Eight cut-outs in the end-cap nearest the detector are covered with 0.5 mm thick titanium (Timetal 15-3 [40]) sheet sealed with o-rings to provide exit windows for particles passing out of the vacuum on their way to the detectors.

Cryogenics are supplied through a cryo-reservoir mounted on the top of the vacuum vessel. This reservoir, patterned after similar devices in Jefferson Lab’s Hall C, contains all the valves, controls, and feedthroughs related to the cryogenic system. It consists of an annular 70 l volume for storage of LN<sub>2</sub> surrounding a 160 l cylindrical LHe reservoir. Both volumes are surrounded by vacuum gaps and are wrapped with MLI. For each of the cryogen circuits, computer-controlled cryogenic valves allow the selection of either thermal siphon flow for normal operation or, to expedite cooldown, direct “forced flow” cooling of the magnet. Control system PID feedback loops adjust the reservoir supply valves, based on liquid level sensor measurements, to maintain the cryogen levels in the reservoirs. The cryo-reservoir also provides the environment for the “vapor-cooled lead” feedthroughs that

provide the transition between the room temperature, water-cooled power leads and the superconducting power buss (see Section 5.2.3).

The spectrometer magnet is mounted on an aluminum base frame, which provides sufficient adjustment to precisely align the spectrometer to the beam line. The entire spectrometer, including the base frame, is mounted on rails which permit the apparatus to be moved off the beam line when necessary.

### 5.2.2. Auxiliary shielding

A major source of background in both the forward and backward modes is radiation showering from the downstream beam line and internal support hardware. On the end-cap through which the particles exit, lead alloy blocks nominally 10 cm thick are installed between the ribs in the region nearest to the central beam tube to shield the detectors from this background and to augment the line-of-sight shielding from the target. In the forward mode, a supplementary block of 5% (by weight) boron loaded polyethylene nominally 35 cm thick is positioned outside these lead blocks to shield against secondary neutrons produced in the beam line and lead shielding. Also in the forward mode, a similar, cylindrical beam line shield of lead and borated polyethylene extends about 400 cm downstream of the cryostat, through the inside hub of the detector support and up to a 130 cm thick wall of iron blocks used to shield the system from radiation backstreaming from the beam dump. The beam line shield is important in reducing detector phototube anode currents to acceptable levels. For the backward angle measurement, electromagnetic background produced inside the cryostat is significantly reduced by a cylindrical shell of lead, 2.5 cm thick, located just inside the central LN<sub>2</sub> shield and extending from the downstream end of the target to the cryostat end-cap.

### 5.2.3. Electrical design

A block diagram of the SMS charging circuit is shown in Fig. 14. Current is provided by a Dynapower 8000 A, 20 V silicon-controlled-rectifier-based supply [41]. A zero-field current transducer is employed to measure the current supplied to the magnet and to provide feedback to the power supply for current regulation. The power supply architecture supports bi-directional power flow allowing the magnet to be both charged from, and discharged to, the power grid. This feature is used to provide a “slow dump” ( $\sim 900$  s) function whereby the magnet current is zeroed by a powered discharge. A “fast dump” capability is provided by a high-speed circuit breaker [42] (rated at 6000 A and 1 kVDC) and an air-cooled high power resistor [43] (rated at 250 V, 5000 A with a resistance of 0.05  $\Omega$ ). Quench detection, as well as a number of safety-related faults, initiate a fast dump. In that event, the fast dump switch opens, disconnecting the power

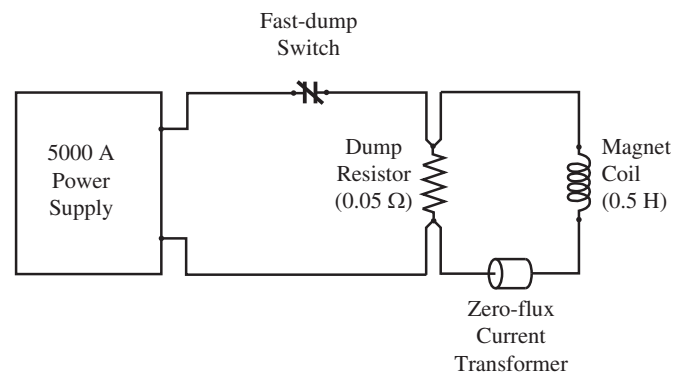


Fig. 14. Schematic diagram of the electrical circuit of the SMS.

supply from the magnet. The stored energy of the magnet, 6.6 MJ at full excitation, is then dissipated by the (parallel) dump resistor with a decay time measured to be 10.4 s.

All interconnections among room temperature components of the circuit are made with either 600 (short interconnects) or 1000 MCM (main magnet connection) flexible, water-cooled cable. Power connections to the superconducting buss are made via vapor-cooled leads (VCLs), which pass through the helium reservoir. They are designed to tolerate the 900 s slow dump after a complete interruption of coolant flow. Each lead consumes 1.8 l/h/kA LHe. The flow of coolant gas is regulated, based on the magnet current, and measured by flow controllers interfaced to the control system. The cold (superconducting) electrical bus connects each coil in series. In order to cancel the field from the cold bus, the current is returned along a path which parallels the supply path.

### 5.3. Tolerances and magnetic field calibration

Studies of the dependence of the SMS forward angle  $Q^2$  resolution on coil profile and alignment, and of the dependence of magnet symmetry and edge scattering effects on collimator position generate a number of manufacturing tolerances for the coils and collimators, listed in Table 4.

The current centroid location (flatness and profile) of each coil was checked prior to assembly by room temperature magnetic field measurements. The assembled coil locations were then verified optically with the magnet both warm and at LN<sub>2</sub> temperature at BWXT using digital photogrammetry, made possible by replacing the Ti exit windows with frames containing optically flat viewports. At Illinois, the coil locations were checked magnetically with the SMS cooled to LHe temperature and running at 20% of full operating current. This test, was performed using a computer-controlled field mapping system [44], which measured the field components outside the cryostat using three-axis Hall probes. The locations of zeros in the field components are determined by making measurements along selected lines just outside of the detector end of the cryostat. The coil locations and orientations are then inferred by fitting the zero locations assuming an ideal model for the individual coils. A final digital photogrammetry check of the coil positions was performed with the magnet at room temperature after it was delivered and installed at Jefferson Lab. These alignment checks are consistent with the tolerances listed in Table 4.

Ultimately, the dependence of the G0 measurement uncertainty on magnet tolerances enters through the absolute calibration of the mean  $Q^2$  associated with the focal plane detectors. This calibration is established in the forward angle mode (and simply transferred to the backward angle measurement) using the ToF difference between pions and elastic protons for each detector. A comparison is made [45] between the simulated and measured ToF differences allowing the magnetic field to vary. Simulation and measurement agree to a precision of 100 ps, which implies an uncertainty on  $Q^2$  within the 1% requirement of the experiment. These results are consistent with the uncertainty in the absolute magnet current measurement.

### 5.4. Control system

The monitoring and control system for the SMS has three principal subsystems: sensors and signal processing electronics (located in a shielded location in the experimental hall), a Programmable Logic Controller (PLC) and its “ladder logic” software, and a console (user interface) computer (located outside the hall in the experiment data-acquisition area). Because of radiation-related faults, the PLC was moved from the shielded area in the experimental hall to the data-acquisition area between the forward and backward angle run periods, communicating by ethernet with a “relay” module remaining in the shielded area.

The signal processing electronics provide conditioning and interface functions (level shifting, gain adjusting, isolation, etc.) for the PLC input/output (I/O). For the most part, the signal processing electronics are packaged in modular DIN-rail-mounted components connected directly to the PLC input/output (I/O) modules. A notable exception are the resistance thermometers, read out using Lakeshore Model 218 temperature monitors [34]. Serial RS-232 outputs from the monitors are converted by a PC-104 single-board computer for direct transfer to the PLC memory via ethernet.

The system is controlled by a Direct Logic DL405 PLC [46]. The PLC program provides the following functionality (using, primarily, I/O modules from the manufacturer):

- analog inputs (cryogen and cold mass temperatures, cryogen pressures, vacuum pressures, valve positions, quench protection voltages, power supply parameters, etc.) are scaled to “engineering units” and stored;
- scaled analog values are compared to operator-set levels and alarm indicators are latched when a level is exceeded;
- based on alarm indicators and digital inputs, interlocks are tripped initiating a fast or slow dump of magnet power;
- cryogenic valve actuators are adjusted according to operator-set values;
- power supply current is adjusted based on an operator-set current and ramp rate;
- gas flow through the VCLs is adjusted either based on operator-set values or automatically, based on current; and
- cryogen level and cooldown (or warm-up) are controlled using PID loops.

The PLC executes its ladder logic program with a cycle time of about 25 ms. However, due to the eight-fold multiplexing of analog input signals, the minimum guaranteed response time is eight times longer, 200 ms. The PLC also serves as a repository for operator-set parameters from the control console. Through a serial connection, all magnet control data are made available to the lab-wide EPICS control system [29]. This allows the status of the magnet to be monitored by accelerator and refrigerator operators and provides a convenient method of including magnet status information in the experiment’s recorded data stream.

The third component of the control system is the console. It runs a dialect of the National Instruments human–machine interface program LookoutDirect [46] during normal operation of the

**Table 4**  
Manufacturing tolerances for the SMS coils and collimators.

Quantity	Value
Deviation of coil current centroid from coplanarity	± 1.0 mm
Deviation in the coil current centroid from the specified in-plane profile	± 2.0 mm
Error in any direction in the location of a coil in the toroid assembly	± 2.0 mm
Error about any axis in the orientation of a coil in the toroid assembly	± 0.15°
Tolerance on the location of any collimator edge	± 5.0 mm

magnet. This console computer, running Microsoft Windows XP, has three main functions. First, it serves as a development station (using DirectSoft32) for the ladder logic program running on the PLC. Second, using screens created with LookoutDirect, one can monitor the status of analog and digital signals, alter operator-settable parameters in the PLC, command the PLC to perform control procedures, and display the logged history of PLC-acquired data. Finally, the console performs the function of logging all monitored data and control parameters to a local, mirrored, hard disk. Data are stored as a function of time in compressed form by LookoutDirect and are available to any Microsoft Open Database Connectivity (ODBC) compatible application.

Quench detection is provided by two parallel systems, a digital PLC-based system and a hard-wired analog system. Both systems are designed to be insensitive to the inductive voltages produced during ramping, and to provide detection of quenches, not only in the coils, but also in the superconducting buss leads. The digital quench protection system is considered a “backup” for the analog system.

Three voltage taps per coil (two on the coil leads and one at the interconnection point between double pancakes), provide a measure of the coil voltage for the quench detection systems. In addition, voltage taps are located on the “transition leads” on the cold side of the VCLs within the LHe reservoir, and about midway between the VCLs and the first coil connection. Finally a diagnostic voltage tap is made at the halfway point on the long return of the cold buss after the last coil.

The analog quench detection system follows a design developed for the CDF [47] and D0 [48] experiments at Fermilab. The magnet forms one half of a bridge circuit. A resistor chain spanning the power supply connections provides the other half. A single quench within the magnet will unbalance the bridge. Isolation amplifier/window discriminator channels sense the imbalance at a threshold of about 350 mV and trigger a fast dump. Additional isolation amplifier/discriminator channels monitor voltage taps across the supply and return superconducting leads, comparing voltage drops to current-dependent thresholds.

Employing isolation amplifiers, the digital quench detection system uses the PLC to examine voltage drops between taps. To accommodate different operating conditions, the PLC compares each voltage to an average voltage derived from all of the coils. A deviation greater than a set threshold of around 200 mV generates a fast dump. Separate thresholds are defined for the transition lead voltage drops, which are also monitored by the digital quench detection system.

### 5.5. SMS performance

Since its installation at Jefferson Lab, the G0 SMS has been operated at full power (5000 A) during several runs extending over many months (forward mode) and then for a period of over a year at lower currents (3500 and 2650 A—backward mode) With only a few exceptions, noted below, it has performed according to the specifications of the original design.

In the reference design, the heat load to LHe is specified to be less than 40 W. However, boil-off studies indicate that the as-built load is about 107 W. The steady-state LHe requirement of the magnet at full power is measured at Jefferson Lab to be about 8 g/s. This is consistent with the measured heat load and some additional load from the supply lines.

Magnet cooldown to LN2 temperature is accomplished by regulating the temperature of helium gas flowing in the cooling circuit through the use of an LN2 heat exchanger. This part of the cooldown requires about 17 days, limited by the cooling capacity of the heat exchanger and by the safety requirement that  $\Delta T$

between inlet and coil average be less than 75 K. Overall, the cooldown typically extended over 21 days, about the twice the original specification.

About 160 of the 3270 h (~5%) of available data collection time during the forward mode commissioning and production running were lost because of problems with the SMS. This represents about 50% of the lost data collection time (the rest was lost due to problems with other systems: target, DAQ, etc.). Most (70%) of the magnet problems were caused by radiation-related faults in control system components located in the experimental hall. The most common problem was the result of non-permanent, radiation-related changes to PLC software that triggered fail-safe logic resulting in a fast dump of the magnet power. Once the PLC program was restored and executing, a minimum of 2.5 h was required to recover LHe level and restore the magnet current. Rest of the magnet-related downtime in the forward measurement was associated with failures of relays used to power the valve motors in the cryogen level control system.

After the PLC was moved to the experiment data-acquisition area, communicating with a relay module interface to the I/O electronics via ethernet, the system was more reliable, because the relay module was much more radiation resistant. The valve control relays were also replaced with a solid-state switching system. With this new configuration, magnet controls problems accounted for about a 1% loss of data collection time.

## 6. Particle detectors

The G0 particle detection system is composed of eight octants of detectors, that count recoil protons from small angle ( $7\text{--}13^\circ$ ) e-p scattering (forward angle mode, initial orientation of the magnetic spectrometer), and scattered electrons from large angle ( $110^\circ$ ) e-p scattering (backward angle mode, second phase of G0 following a  $180^\circ$  rotation of the spectrometer).

For the forward angle measurements, there are 16 detectors in each octant lying on, or near, the focal surface of the SMS magnet. These FPDs detectors (see Fig. 15) consist of pairs of plastic scintillators, contoured to define a specific range of  $Q^2$ . The first 14 detector pairs each measure a rather narrow range of  $Q^2$  values

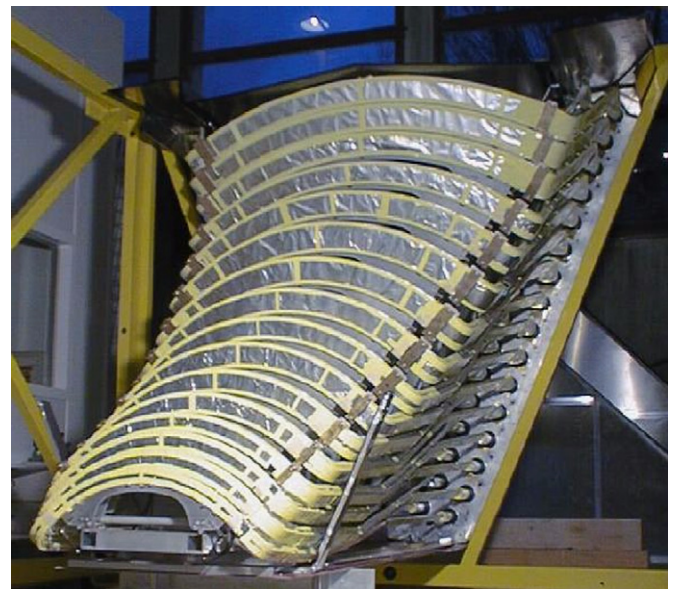


**Fig. 15.** Photograph of one FR FPD octant. The FPD numbers (1–16) increase from the bottom to the top. The scintillators are the arc-shaped segments lying in (nearly) vertical planes. Light guides from the ends of the arcs lead to phototubes at the back plane of the mounting structure.

of the recoil proton for e–p elastic scattering in the domain  $0.12\text{--}0.55\text{ (GeV}/c)^2$ . As mentioned in Section 2.2, most of the background from inelastic protons and pions in these detectors is eliminated by measuring the ToF of the particles to the detectors. By contrast, detector 15 collects recoil protons over the  $Q^2$  domain from 0.55 up to approximately  $0.9\text{ (GeV}/c)^2$ . For this detector the ToF serves as a measurement of the momentum of the proton, and thus the  $Q^2$ . Because of the “turnaround” of the higher energy protons (Section 2.2), the yield for elastically scattered protons with a  $Q^2$  near  $1.0\text{ (GeV}/c)^2$  actually falls on FPD 14, but at a very different location in the time spectrum. Finally, the 16th detector serves as a monitor of backgrounds and the spectrometer field.

For the backward angle electron scattering, the kinematics are such that a single  $Q^2$  value is measured for each incident beam energy. In the case of the backward angle measurements, ToF is no longer useful in terms of separating the elastic, inelastic and pion events, since the flight time is essentially the same for these relativistic particles. Instead, a second array of nine scintillators is added near the exit window of the magnet cryostat for each octant. As discussed in Section 2.3, these CEDs are used in coincidence with 14 of the 16 FPDs in order to define the trajectory of the particles. Using different sets of CED–FPD pairs, electrons from elastic e–p scattering can be separated from those associated with inelastic scattering. Simulations and analysis of test data [49] indicated the need to add a Cherenkov detector to each octant to discriminate electrons from pions. This particle identification is crucial for the measurements with the deuterium target, since there is a large yield from negative pions produced from interactions with the neutrons.

### 6.1. Focal plane detectors

The FPD scintillators are arch-like shapes which are defined by tracing an array of proton rays, from elastic e–p scattering, through the SMS magnetic field using TOSCA [50] and specialized fast tracking codes. Specifically, based on simulation, elastic e–p scattering  $Q^2$  bins are chosen to provide reasonable resolution and to produce roughly equal count rates, at least up to about FPD number 11, above which the e–p elastic rates are reduced and the detector widths are chosen on the basis of momentum resolution. Rays are generated for three positions along the 20 cm cryotarget (front, middle, and rear) and for three azimuthal angles  $\phi = 0.0^\circ$ ,  $5.0^\circ$ , and  $10.5^\circ$  (the rays are symmetric about the center of the octant,  $\phi = 0^\circ$ ). The azimuthal acceptance for each octant is limited to  $\phi = \pm 10^\circ$  by the upstream collimators in the SMS magnet, and  $0.5^\circ$  is added to account for possible misalignment of these collimators. To design each of the first 13 FPDs, the rays corresponding to the lower and upper boundaries of the  $Q^2$  bin are projected onto an  $x$ – $y$  plane at the  $z$  location of the focal surface for that  $Q^2$  and the central ray  $\phi = 0^\circ$ . For the central rays, the  $x$ – $y$  positions for the three target positions coincided, as expected for the SMS design. However, for non-zero  $\phi$  angles the positions differ by a few mm due to changes in the magnetic field near the coils. After examining various descriptions for the shapes of the detector boundaries and their effect on the  $Q^2$  resolution, we concluded that detector boundaries in the  $x$ – $y$  plane are satisfactorily described by arcs of circles with the center and radius chosen from a fit to rays corresponding to the three azimuthal angles and originating from the center of the target. The lengths (azimuthal extent) of the counters are then determined from the most extreme rays, which originate from the upstream end of the target at  $\phi = 10.5^\circ$ , to which approximately 1 cm in length is added to compensate for multiple scattering and possible misalignment (2 mm) of the detectors. Typical dimensions of the scintillators are 60–120 cm in length and 5–10 cm in width. Finally, the defined detector shape is rotated by a few

degrees about the  $y$ -axis so particles enter perpendicular to the detector, at least at its center. This is done to reduce double hits on the FPDs. For detectors FPD 14 and 15 the same basic procedure is followed; but as discussed above, the one-to-one correlation between focal plane position and  $Q^2$  disappears at larger  $Q^2$ . There is a turnaround of the ToF versus  $Q^2$  elastic locus as the momentum becomes relatively larger and the recoil angle smaller, and both detectors count protons from a range of  $Q^2$  values of the recoiling protons. Note that FPD 16 is chosen to have a shape identical to that of FPD 15, since it serves as a monitor for background. The final detector design is done with TOSCA-based software, the end result being a file for computer-controlled machining.

Each of the FPD scintillators is paired with a second identically shaped partner to reduce background from neutral and low-energy particles. In the interest of redundancy and time resolution, for the forward angle measurement, the two ends of each scintillator are viewed with a photomultiplier tube (four PMTs for each scintillator pair). With less strict timing requirements, the backward angle measurements utilized the same scintillator pair, but with only one PMT on each member (e.g., at the left end of the front detector and the right end of the back detector). Lucite light guides are used to transmit the light produced in the scintillator to photomultiplier tubes mounted in a region of low magnetic field—as much as 2 m away for the low  $Q^2$  FPDs (see Fig. 15). The high density of light guide material on the sides of each detector pair required significant design time to overcome interferences between the various components. The length and thinness of the scintillators and light guides led to concerns about the number of photoelectrons from the photomultiplier tubes, but a set of simulations and experimental studies were undertaken to confirm that a satisfactory number of photoelectrons would be produced by minimum ionizing particles.

Internal alignment to 2 mm of the 16 scintillator elements making up a single octant is carried out when the octant modules are assembled. The alignment of FPD octant modules relative to the magnet and electron beam is accomplished with adjustment degrees of freedom provided by the detector octant support frame.

For several reasons, based on budgetary constraints and on technical and scientific grounds, the detectors and electronics for the four octants numbered 1, 3, 5, and 7 were built by a North American (NA) collaboration (USA–Canada), and those for octants 2, 4, 6, and 8 were built by a French (FR) collaboration. Although the basic elements of the detector systems are identical, there are differences in the details of the design and the construction procedures. The important differences are described in the following two subsections. Note that the assigned octants for each collaboration are opposite to each other in azimuth, in order to reduce possible systematic errors.

#### 6.1.1. North American FPD detectors

The NA scintillation detectors are made from Bicron BC-408 [51]. The FPD 5–16 pairs are fabricated from 1 cm thick scintillator sheets, whereas FPD 1–3 are fabricated from 5 mm scintillator to accommodate the lowest energy protons. FPD 4 consists of a 0.5 cm front layer followed by a 1 cm rear layer of scintillator. The scintillator pairs are separated by identically shaped 3 mm thick polycarbonate sheets to provide additional absorption of low-energy particles. All scintillators are initially rough machined to the approximate shape (1.5 mm oversized) using water jet cutting. Five of these scintillators are then stacked, and the curved sides milled on a CNC machine. The machined sides are hand polished. The quality of the polished surface for each detector is tested using an automated laser reflection technique, and several were re-polished to improve performance. In the final step each scintillator is wrapped using strips of aluminized mylar. It is not

necessary to make this wrapping light-tight, since the octant support is designed as a light-tight box.

The NA light guides are fabricated from UVT transmitting lucite (Bicron BC-800 [51]). Due to the complicated geometry of the light guides, it was necessary to develop a series of jigs and bending techniques. Silicone “cookies” are used for coupling the light guides to the phototubes.

Once the scintillators and light guides are fabricated, they are mounted and glued on the final precision support structure at Jefferson Lab. After assembly, careful tests of the performance of each detector are made. Specifically, a  $^{106}\text{Ru}$   $\beta$  source is placed at several locations along the length of the scintillator and the light output measured. The design goal is to obtain  $\geq 100$  photoelectrons for proton detection and  $\geq 50$  photoelectrons for electron detection for the worst case, i.e., when the source was on the far end of the scintillator away from the phototube. In all cases this goal is exceeded by about a factor of two. In addition to the source tests, prior to sealing the light tight box, data were taken for cosmic rays, permitting one to monitor possible deterioration of the scintillators, light guides, and/or photomultiplier tubes over time.

The phototubes for the four North American octants are 12-stage Photonis [52] XP2262B tubes. All tubes were tested for non-linearity and their gains measured with the results stored in the experiment database. The design of the PMT base takes into account the relatively large dynamical range required by the experiment (light output from minimum ionizing electrons to that of 60 MeV protons). The bases are passive, being made up of resistors and Zener diodes, and include a Zener-assisted front stage to maintain collection efficiency of the primary photoelectrons, independent of the operational setting of the photomultiplier tube. The photomultipliers are also equipped with  $\mu$ -metal magnetic shielding.

To transport the signals from the PMTs in the experimental area to the electronics, approximately 150 m of coaxial cable is used. This leads to significant attenuation in the signals, which in turn necessitates either operating the tubes at a higher voltage (leading to more anode current), or introducing an extra stage of amplification. Due to concerns about high anode currents reducing the lifetime of the PMTs and the long running time needed to carry out the G0 experiment, amplifiers with gains of approximately 25 (Phillips model 776, modified to increase gain from 10 to 25) were introduced in the experimental area. This addition maintained the anode currents in an acceptable range.

### 6.1.2. French FPD detectors

The FR detectors are similar in many respects to the NA detectors; only key differences are highlighted here. They are also fabricated from BC-408, in this case obtained from Eurisys, a European subsidiary of Bicron [51]. The FPDs 1–3 are 5 mm thick and FPDs 4–16 10 mm thick. The scintillator pairs are separated by identically shaped 3 mm thick aluminum sheets. The light guides, made of acrylic, were machined by a contractor in straight sections and bent directly onto the mechanical support structure. Additional parts of the light transmitting system (fish tails and PMT adaptors) were also made commercially and later glued to the light guides. The most robust joints were glued and the scintillators and light guides were then wrapped with aluminum foil.

Before the material was shipped to Jefferson Lab, a complete test assembly of one octant was done in France, in order to check the procedure and to identify possible interferences. Using cosmic rays, photon yield measurements are made at three locations along the scintillators. The absolute normalization is done using the single-photoelectron signal from a photodiode. The French FPD detectors generate essentially the same number of photoelectrons as

compared to the NA design. The final operation, the gluing of the more delicate joints, took place at Jefferson Lab. Optical grease was used to couple the PMTs and light guides.

For the FR FPDs, lower gain, 8-dynode Photonis XP2282B tubes [52] are used and specified to have small gain dispersion. This feature simplifies the gain adjustment through variation of the high voltage. After tests, it is indeed found that the gain variations measured are less than a factor of 4.

For the photomultiplier bases, a built-in amplifier (gain of 20 overall) is included in the design. The anode currents are thus kept to values of a few  $\mu\text{A}$  without additional amplifiers, allowing the long term operation of the tubes needed by the G0 project. Following irradiation tests of components (see next section), Zener diodes were chosen instead of transistors for gain stabilization in the electrical design. A base-line restoration function is also included in the design. In addition to the  $\mu$ -metal magnetic shielding, an electromagnetic shield consisting of a metallic copper sheet rolled around the plastic housing is incorporated to decrease the noise on the PMT signal.

The octant support is a welded aluminum tube structure, designed to align the detectors to within 2 mm of their optimal locations. In order to save weight, the back plane is made of two 20 mm thick beams that form a V-shape. Finite element analysis was carried out to ensure acceptable deformations of the support structure. Finally, a dedicated aluminum structure holding a Tedlar cover is integrated in the design to ensure the octant is light-tight.

## 6.2. Radiation damage tests

Prior to construction, extensive neutron irradiation tests of the light guide material and of different types of glue were performed at a dedicated facility in Orleans (France). Two 5 mm thick pieces of acrylic were glued together and irradiated by a flux of  $5 \times 10^{13}$  to  $10^{14}$  n/cm<sup>2</sup> 6 MeV neutrons. The electronic components for the French bases and the silicone cookies used to couple the North American PMTs were also tested. The results showed that, after irradiation:

- attenuation of light by the glue and the silicone cookies varies from negligible up to 5%;
- increased attenuation of light in the acrylic could reach 20% around 400 nm for large neutron doses (with the implication that during the time between G0 runs when other high-intensity experiments are performed in Hall C, the detectors must be properly shielded); and
- the Zener diodes, and the base-line restoration and amplifier transistors used in the FR bases suffered no degradation (total of  $7 \times 10^{14}$  n/cm<sup>2</sup>).

## 6.3. Anode current measurements and PMT protection circuit

Particularly for the forward angle measurement, there was concern about background events in the detector PMTs with amplitudes below the discriminator threshold, but which contribute significantly to the photomultiplier tube anode current. This anode current should be kept below about 50  $\mu\text{A}$ , with an absolute limit of 200  $\mu\text{A}$ , in order to limit gain changes due to PMT aging during the experiment. Under normal operation about 90% of the anode current is due to sub-threshold events, mainly due to GHz-rate single-photoelectron events. This high background rate results in a nearly DC background anode current, requiring reduction of the PMT gain and use of additional amplifiers of gain 20 (FR detectors) and 25 (NA detectors) so as to obtain the necessary amplitude for proton signals at the discriminators.

To continuously monitor the anode currents, we use the average signal height as measured in the monitor ADC spectra (see Section 7.3), including events below the threshold of the main, time-encoding electronics. During data-taking, a part of the acquisition code determines the average of each ADC spectrum after a user-selected number of events, subtracts the results obtained without beam, applies a calibration factor and produces a bar graph of the anode currents for all detectors. The algorithm can average backwards in time with a user-selected decay constant to smooth out fluctuations.

The calibration factor is determined by measuring the anode current for selected tubes with a pico-ammeter (a) directly at the PMT and (b) after the amplifier. To obtain the amplified anode current and to correct for the amplifier DC offset, the PMT high voltage is cycled on and off.

Under certain conditions, the anode currents can increase dramatically, for example, when diagnostic devices are inserted into the beam line or when the SMS current is zero. In order to protect the PMTs from damage under these circumstances, an electronic “high voltage shutdown” circuit is included in the detector system. It has analog inputs from eight selected PMTs, as well as logic signals from the SMS and Møller polarimeter magnets. The analog inputs are integrated with a time constant of 0.5 s (which approximates the time constant for PMT damage) and with a threshold at approximately twice the desired maximum anode current.

In addition, the anode current of a test, “paddle” scintillation detector, is monitored. Placed near the main detectors, it serves to continuously indicate the general beam quality, especially when the main detectors are turned off.

#### 6.4. Cryostat exit detectors

As noted above, since ToF is no longer useful at the backward angles, the CEDs are required for to separated elastic and inelastic events in the G0 backward angle phase (see, for example, Fig. 3). The array of nine CEDs in each octant is used in coincidence with the top 14 of the 16 FPDs. The CED/FPD combination correlates the momentum and scattering angle of the detected electrons, and thus allows for the separation of elastic and inelastic events. With front-end electronics composed of gate arrays, it is possible to record events for each CED/FPD pair, and thereby measure asymmetries for both elastic and inelastic events.

Constrained by the general shapes of the FPD scintillators, the CEDs are also arch-shaped detectors. They are 1 cm thick BC-408 scintillators coupled to BC-800 UVT light guides [51], and are viewed from each end by the same photomultiplier tubes as used for the FPDs. The CED light guides have shapes similar to the FPD light guides, primarily involving a tight “helical bend” which guides the light from a high-field, geometrically constrained region, to a lower-field region approximately 1.5 m away where the photomultiplier tubes are located.

The photomultiplier tube arrangement for the CEDs is similar to that used for the FPDs. In fact, because of the extra detector in the coincidence (the CED), we were able to remove one phototube from each element of the FPD pair and reuse them for the CEDs. A detailed simulation of expected light yield from the CEDs was done and tests performed on prototypes. The expected number of photoelectrons produced was found to be greater than 50 for minimum ionizing electrons for each of the two PMTs. Tests using cosmic muons, performed after assembly at Jefferson Lab, showed that these numbers were conservative.

The design of the octant support structure for the CEDs takes into account both the required mechanical support of the CED scintillator/light guide/PMT and base assemblies, as well as the relatively weak alignment constraints on these detectors. Because

of their physical proximity, an integrated design for the CED-Cherenkov support subsystems is used. The support structure centers around the use of prefabricated aluminum extrusions from Bosch [55] because of their strength, versatility, and relatively low cost. A series of detailed finite-element analysis studies was carried out to identify potential problems and to optimize the strength and cost of the support structure.

#### 6.5. Cherenkov detectors

An aerogel Cherenkov detector is used to reject  $\pi^-$  background from  $n(e,\pi)$  reactions and is especially important for the backward angle quasi-elastic scattering of electrons from the deuterium target. The detector operates in coincidence mode for the electron detection, and in veto mode for background studies and pion measurements. It is designed to reject pions over the full G0 momentum range, i.e., beyond a minimum of  $\sim 400$  MeV/c. Eight such detectors were constructed and mounted between the CEDs and FPDs of each octant.

The electrons and pions pass through 5.5 cm of clear SP30 aerogel [56]. The aerogel has an index of refraction of  $n=1.035$ . With this index, all primary electrons produce light, but pions below about 570 MeV/c do not. The light is emitted within a small angle cone ( $\sim 15^\circ$ ) and enters a downstream region whose walls are lined with a white diffuse reflector, GSWP 00010 paper [57]. This light is collected by four XP4572B phototubes from Photonic [52] (see Fig. 16). The fraction of the light collected by the phototubes is about 4% of that produced in the aerogel. The other goals in the design are to cover as large a fraction as possible of the G0 acceptance, while keeping the timing spread as narrow as possible and the collection efficiency of the photons by the tubes independent of the position of the particles to be identified. Studies with both Monte Carlo simulation [53] and prototypes of the Cherenkov counter were carried out in France and in North America. Prototypes were tested with cosmic muons and using

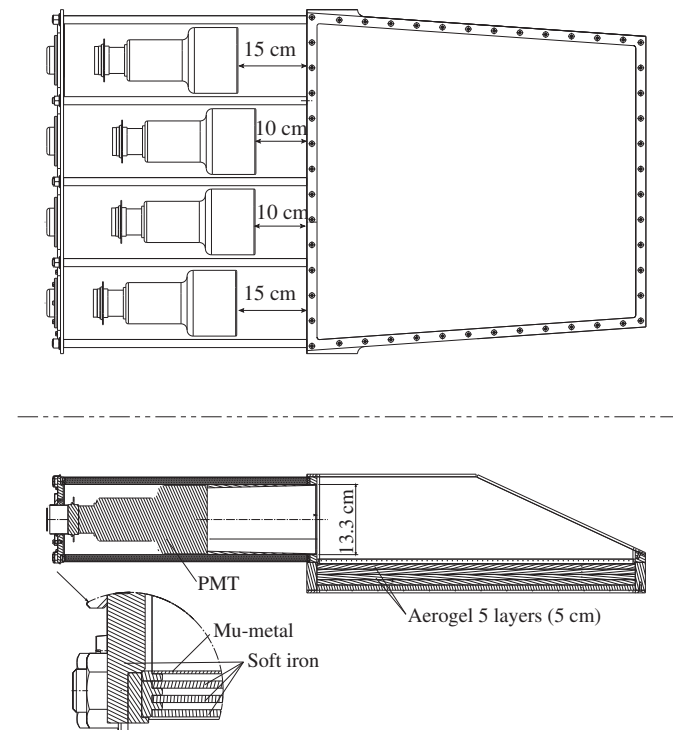


Fig. 16. Schematic of a Cherenkov counter—beam view and section. Both the magnetic shielding and the varying phototube set-back distances are necessary to cope with the fringe field from the SMS.

test beams at TRIUMF. A mixed particle test beam was used to measure the pion–electron discrimination, and the M11  $\beta \sim 1$  electron beam line was used to measure the position dependence of the overall measurement efficiency. Electrons are found to generate a signal of 6–7 photoelectrons. With such numbers, the detection efficiency for an electron is close to 95%, whereas a 400 MeV/c pion has a rejection factor of 125–1. The pion “signal” is, in fact, mostly due to  $\delta$ -rays produced in the CEDs and the Cherenkov structure.

The four phototube signals in each counter octant are combined together, typically with a 2/4 coincidence requirement. This signal is discriminated and used in the trigger. The typical time-width of the signal is  $\sim 20$  ns (due mainly to collection time in the light box), and the rise time of the pulse is  $\sim 1$  ns. ADC spectra for the individual tubes are recorded by the monitor electronics and used to check the calibration and pion contamination factor of each octant.

Magnetic shielding is important for the operation of the phototubes in the Cherenkov detectors because their sensitivity is reduced by a factor two when operated in a region with a field as low as 0.1 mT. During the G0 experiment, these tubes encounter maximum field components of the order of 4 mT in the axial direction and about 11 mT in the transverse direction. Such relatively high fields require efficient shielding. Tests under similar field conditions were thus performed at the Grenoble High Magnetic Field Laboratory. The configuration chosen (see Fig. 16) was tested and shown to achieve the required shielding under the G0 running conditions. It consists of three 45 cm long concentric tubes of 0.3 cm thick soft iron and one of 0.5 mm thick Mu-metal (permeability of about  $8 \times 10^4$ ) surrounding the photomultiplier tube and capped by a square soft iron plate at the socket end of the tube. It is necessary to isolate the  $\mu$ -metal tube from the square plate in order to break the magnetic circuit. With this shielding, no significant loss in gain is measured for the nominal G0 magnetic field. In addition, these tests also permitted us to optimize the position of the PMT relative to the counter body and adopt a set-back of only 10–15 cm. Compared to the initial design with a 20 cm set-back, this provides a significant (of order 30%) increase of the total number of photoelectrons collected by the tubes.

The original borosilicate photomultiplier tubes in the Cherenkov detector were eventually replaced with quartz-faced tubes because of neutron backgrounds (especially prominent in the deuterium running). Low-energy neutrons capture on the  $^{10}\text{B}$  in the tube faces and sides, producing  $\alpha$  particles whose scintillation is detected by the tube. Using tubes with quartz faces (special order, similar to Photonis XP4572B [52]) reduced the background signal rate by slightly more than a factor of two.

### 6.6. Gain monitoring system

In order to track relative variations in the pulse-height and time response of the scintillator-based detector system, a gain-monitoring system (GMS) is used. The underlying design of the system is similar to those found in many other experiments [54]: a light source generates a short burst of photons that are distributed to the scintillator elements via optical fibers. Originally, the system was based on a fast nitrogen laser (pulse length  $< 1$  ns), but the reliability of these lasers did not prove sufficient for our needs, and the very short pulses proved unnecessary, so in the final implementation a nitrogen flashlamp is used. The distribution of wavelengths produced by the flashlamp has a maximum intensity in the ultraviolet, near 350 nm. A tail extends through the visible; the intensity at 800 nm is about 15% of that at 350 nm. Wavelengths below 200 nm are cut off by the exit window of the lamp. The light from this lamp encounters a

rotating mask that permits the light to fall upon 1 of 15 clusters of optical fibers. The mask rotates continuously; a set of switches indicates the location of the mask, and associated electronics control a “mask ready” signal used to make sure the flashlamp will only be fired when the mask is in a valid position. Each of the 15 clusters behind the mask contains 19 optical fibers. The fibers are arranged so that, for example, one of either the “left” or the “right” end of each FPD scintillator element is fired at a time. The comparison of the response of the scintillator and phototubes to these left and right pulses is used to monitor changes in the condition of the scintillator separately from changes in the individual phototube gains.

The flash lamp intensity varies significantly from one pulse to the next. An additional cluster of seven fibers is therefore positioned behind a hole at the center of the mask and illuminated on every firing of the lamp. Some of these fibers are connected to small scintillators attached to the window surfaces of phototubes, whose signals are used to correct for the pulse-to-pulse behavior of the lamp. These phototubes are protected from the large flux of charged particles present in the experimental hall. One scintillator in this referencing subsystem contains approximately 0.6 nCi of  $^{241}\text{Am}$ . The  $\alpha$ -decay from the source produces light pulses used to monitor the drift in the gain of this reference detector.

The optical fibers used are pure silica (core and cladding), allowing for the transmission of ultraviolet light over a long distance, and making them resistant to the very high radiation environment in the experimental hall. By transmitting ultraviolet light directly to the scintillator, one takes advantage of the resulting conversion into blue light via the fluorescence effect which is very similar to the process of scintillation. This provides a uniform illumination of the detector volume in a way that is similar to that from the passage of a charged particle.

The mask is rotated so mask ready signals are produced at a rate of about 2 Hz. The mask is “ready” for a period of about 70 ms each time. The actual firing of the flashlamp is controlled by the data-acquisition system which, upon detecting the presence of a new “mask ready” signal, waits until the next helicity flip period (occurring approximately every 33 ms and lasting only 500  $\mu\text{s}$ ) to fire the lamp. Thus, the flashing of the lamp and subsequent collection of GMS pulse-height and timing data occurs during a time when no asymmetry data are being collected.

The GMS provides only a relative gain reference; its final configuration (nitrogen gas pressure, plasma discharge voltage, and trigger timing) was determined along with the configuration of the rest of the detector system during our engineering runs. After the relationship between the GMS response and the general detector response to the charged particles is established, the GMS provides a way of monitoring the state of the scintillator transmission length and phototube gains. The GMS also proved to be useful in the times between beam use periods, when configuration changes to the detector and/or data-acquisition system needed to be checked.

## 7. Electronics and data acquisition

The different requirements of the forward angle and backward angle modes of the G0 experiment lead to rather different configurations for the electronics used to process the signals from the detectors. As discussed in Section 6, the detectors and electronics for octants 1, 3, 5, and 7 were built by a North American (NA) group, and those for octants 2, 4, 6, and 8 were built by a French (FR) group. Because of differing backgrounds and expertise, significantly different solutions for the electronics are

adopted by the two groups, particularly for the forward angle measurement. In this section we first summarize common aspects and the individual features of the forward angle electronics [8], followed by a description of the common aspects of the backward angle configuration, again supplemented by separate presentation of the two specific designs. Note that the use of two almost independent designs for the electronics provides a valuable tool to search for false asymmetries or other artifacts that might be introduced by problems in the electronics and that could thereby compromise the physics result of the experiment. The results of both the forward and backward angle modes of the experiment are completely consistent between the two sets of electronics, yielding no indication of such a problem (see, for example, Fig. 18 of Ref. [8]).

### 7.1. Forward angle electronics

In the forward angle measurement, ToF from the target to the detectors is used to separate the elastic protons from inelastic protons, pions and other background. Because of the high rates of a few MHz in each channel (FPD pair), time-encoding electronics (TEE) builds ToF spectra for each channel in hardware scalars; the spectra are stored by the data-acquisition (DAQ) system using the standard readout controllers (ROCs) that are part of the Jefferson Lab CODA system [58] (see Section 7.4).

Signals from the detectors proceed first to a patch panel in Jefferson Lab Hall C through RG58 cables (total length of 36 m). From there they propagate to the electronics counting room through 107 m long RG8 (for reduced attenuation) cables. At that point, the signals are split into two signals leading to the monitoring (Fastbus) electronics and the TEE. The NA setup uses passive splitters, delivering 1/3 of the signal to the monitoring electronics and 2/3 to the TEE. The FR electronics uses active splitters with unity gain in both channels so there is no loss of amplitude. The monitoring electronics system is based on commercial ADC and TDC units in Fastbus crates and is common to both the NA and FR setups. It gives precise event-by-event information on the pulse height and time response of the detectors, but is highly pre-scaled to reduce the rate to a manageable level ( $< 1$  kHz).

The front-end of the TEE consists of Constant Fraction Discriminators (CFDs), Mean-Timers (MTs) and a coincidence unit. Since off-line walk corrections are prohibited by the lack of event-by-event data, CFDs are chosen in order to provide good time resolution over a large dynamic range, the zero-crossing being independent of the amplitude of the input signal. To reject low-energy background, the CFD thresholds are set to 50 mV. The two CFD output signals associated with the left and the right PMTs of a given scintillator are mean-timed, so the timing of an event delivered by the MT is independent of the hit location on the scintillator paddle. When a coincidence between the MT signals associated with the front and back scintillators of a given pair is obtained, the event timing is encoded and the corresponding bin of the ToF spectrum is incremented.

As mentioned earlier, the beam time structure of the G0 beam for the forward angle mode is chosen to be 31.1875 MHz (499 MHz divided by 16), and so there is one beam pulse (“micro-pulse”) every 32 ns. The start of the ToF is generated by a signal,  $Y_0$ , from the RF pulse of the electron beam as it passes through a microwave cavity just upstream of the target [59]. As detailed in Section 3.3, the helicity of the beam is flipped at 30 Hz so that one helicity state, referred to as one macropulse (MPS), lasts 33 ms. The readout of the TEE data (ToF spectra) is performed at the end of each MPS, during the helicity flip which takes about 500  $\mu$ s. The selection of elastic events, as well as the calculation of all asymmetries, is performed during off-line analysis.

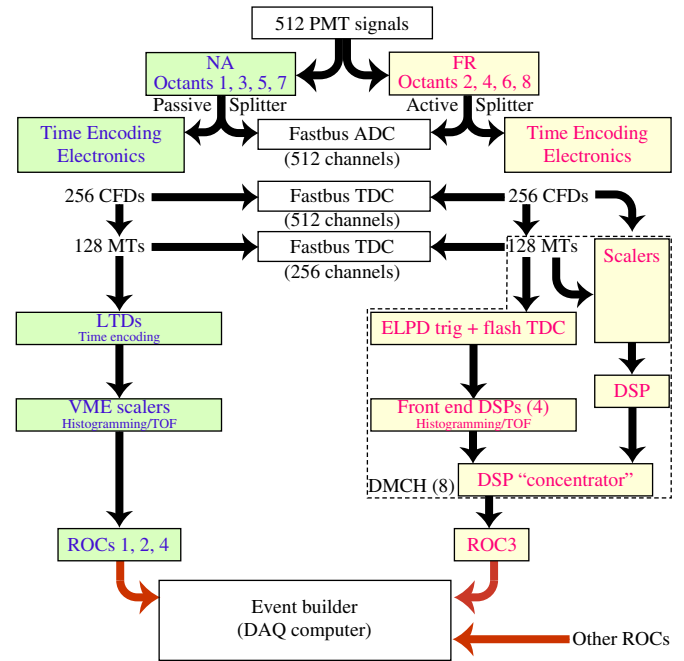


**Fig. 17.** Schematic of the forward angle detector electronics showing the NA and FR branches. ToF is measured and recorded in different ways in the two cases (see text).

In normal data-taking the DAQ integrates each helicity state for two cycles of the AC line period, i.e., for 1/30 s. This cancels any noise at the line frequency or its harmonics. To ensure that substantial line noise is not present, occasional dedicated runs are performed in which each 1/30 s helicity state is integrated as four 1/120 s parts. These runs show negligible 60 Hz contributions.

As mentioned, two rather different solutions are adopted by the NA and FR collaborations for the time-encoding electronics. The NA electronics is modular and based on a combination of commercial and custom-made elements. It is robust, but has limited binning size (1 ns), due to the limitation of the maximum clock speed associated with the technology employed. The FR electronics, by contrast, is highly integrated and has time resolution of 250 ps, making some tasks, such as background correction, easier. A block diagram showing the entire electronics chain is shown in Fig. 17.

The same two schemes are implemented in each design to reduce helicity-dependent effects related to deadtime: the Next-Pulse-Neutralization (NPN) and the “buddy” method. The probability of one event being detected in a single micropulse is 3% at 1 MHz. In order to allow the signals to completely clear the mean-timer, the encoding is disabled for the next micropulse (32 ns later). This increases the deadtime by a few %, but in a controlled, deterministic way. The buddy method permits the study of the deadtime for each detector by recording how often one detector records a hit when its buddy (the same detector number located in the opposite octant of the detector array) is busy. This quantity is monitored in particular for indications of helicity-correlated structure in beam intensity, which would be seen as a helicity-correlated variation in these buddy rates. This permits us to monitor for helicity-correlated deadtime losses which might introduce a false asymmetry. For the FR electronics it is also possible to use the buddy method for each bin of a ToF spectrum, e.g., for the elastic peak (“differential buddy”).

#### 7.1.1. NA electronics—forward angle

The NA electronics system uses separate modules to perform the tasks of discrimination, mean-timing, time-encoding, and ToF

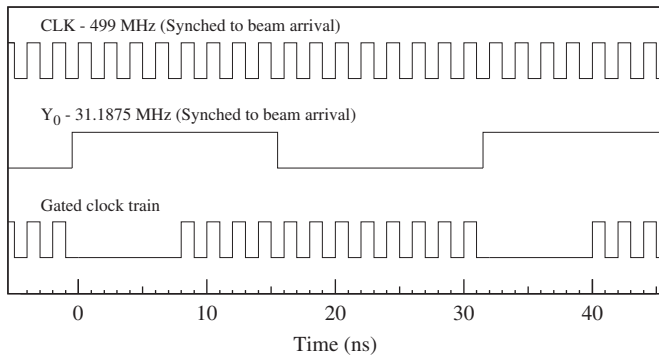


**Fig. 18.** Timing diagram showing gated clock trains generated based on the free clock (CLK) and beam arrival ( $Y_0$ ) signals for the NA electronics, as described in the text.

spectrum accumulation. Additional modules are used to generate the clocking signals used by the time-encoding boards.

Commercial LeCroy 3420 CFDs [60] are used to minimize time-walk in the PMT anode pulses. Custom mean-timers, utilizing the same application-specific integrated circuit (ASIC) as in the FR electronics, are then used to average the pulse times of the PMTs at the opposite ends of each scintillator. The ASICs introduce the two signals into counter-propagating shift registers and generate a mean-time signal when a coincidence occurs. Copies of the CFD outputs and of the mean-timer outputs are also sent to the monitoring electronics.

Mean-timed signals from the focal plane detectors are sent to the time-encoding boards, the “Latching Time Digitizers” (LTDs). First, a coincidence is required between the front and corresponding back detectors, with the timing being determined by the front detector. The ToF is determined using a clocked shift register, a very simple method for accumulating time spectra for data rates of several MHz. With an overall cycle time of 32 ns, an externally generated train of 12 clock pulses, synchronized to the  $Y_0$  signal (see Fig. 18) is used to clock a shift register whose input is latched on by the front-back coincidence. The depth of penetration of the input signal into the shift register during the shifting sequence then depends upon the time of the coincidence within the 32 ns cycle. The depth of penetration of the signal thus encodes the time of the coincidence. A time spectrum can then easily be recorded by presenting the parallel output bits from the shift registers to individual scaler channels. Scaler channels corresponding to times subsequent to a coincidence are incremented while those corresponding to earlier times in the 32 ns cycle are not. The shift register input is latched through the remainder of the clock train to simplify extraction of the time spectrum from the scaler information by taking differences of successive scaler channels. After a period of accumulation, each of these differences represents the number of coincidences which came within a time bin early enough to increment one scaler channel but not early enough to increment the next channel.

The CLK and  $Y_0$  signals are sent to a custom board, the clock-gating board, which gates off a group of four pulses of CLK, synchronized to  $Y_0$ . The resulting 12-pulse clock trains are duplicated by custom signal-duplication boards and distributed to the LTDs to act as the time base for ToF measurements. Restricting the clock train to 12 pulses allows us to record only the times of interest (starting at the time when the fastest particles reach the detectors).

The LTD boards incorporate a few refinements of the basic mechanism described above. In fact, the latched input signal is presented to the inputs of two shift registers, one of which is clocked by the leading edges of the clock train and one of which is clocked by the trailing edges. This effectively halves the time

bin size since interleaved differences can be taken between a scaler channel on one shift register and one on the other. The clock pulse frequency is 499 MHz, so this interleaving reduces the time-bin width from roughly 2 ns down to roughly 1 ns. The input latch is not simply reset at the end of each clock train. Rather, if it is set in a particular clock train, it is cleared at the end of that clock train and also disabled for the duration of the subsequent clock train. As noted above, this enforced, extended deadtime is intended to make deadtime corrections more accurate by reducing dependence on the less well-defined deadtime properties of PMTs, CFDs and mean-timers. Each LTD encodes times from two front scintillators (buddy pairs).

### 7.1.2. FR electronics—forward angle

The FR electronics consists of eight custom mother boards called DMCH-16X (Discrimination, Mean-Timing, time enCoder, Histogramming, 16 Mean-Timer channels within the VXI standard), each handling the eight detectors (32 PMT channels) of half an octant. Because of integration, the electronics for four octants fits in a standard, C-sized VXI crate. An interface module provides common signals (MPS,  $Y_0$ ) to the DMCH-16X boards through the VXI back plane. One DMCH-16X board consists of the following:

- 32 CFDs<sup>43</sup> and 16 MTs grouped into 16 CFD-MT daughter boards, each of them holding two CFDs and one MT;
- 4 EPLD-Trig (Electrically Programmable Logic Device for Trigger) modules dedicated to logic, in particular the coincidence between front and back MT signals;
- 2 custom numerical time encoders locked to the  $Y_0$  signal;
- 4 asynchronous First-In-First-Out (FIFO) buffers (2048 words) to hold the events on the way from the time encoders to the front-end Digital Signal Processors (DSPs);
- 4 front-end DSPs (ADSP-21062 SHARC [61]) for histogramming;
- a Field Programmable Gate Array (FPGA) chip and a DSP grouped onto a daughter board (“SDMCH”) to provide individual CFD and MT scalars independent of the ToF data;
- 1 DSP concentrator (ADSP-21062 SHARC) which collects data from the 5 DSPs, and
- an internal signal generator (“GDMCH”) for testing the CFDs and MTs.

A schematic of the architecture of the DMCH-16X mother board is presented in Fig. 19.

The processing sequence begins as each CFD, after an input signal, is disabled until the end of the mean-timing sequence. Based on the longest scintillator paddle, the MT compensation range is set to 17 ns; the overall MT deadtime is about 37 ns. The front MT signals are used to set the overall timing. To achieve better time matching between the front and the back MT signals, a software-controlled, internal delay can be adjusted. This delay can be set from 0 to 44 ns in 0.175 ns steps. The coincidence window, which is generated by the EPLD-Trig once a back MT signal arrives, is set to 7 ns. Apart from the coincidence logic, other modes have been implemented in the EPLD-Trig chip that can be selected by software for testing purposes. These test modes allow one to build ToF spectra of only front signals, only back signals, or of both. The NPN and the Buddy schemes can also be disabled for testing purposes.

The numerical time encoder is an ASIC with 250 ps time resolution and a start time (the  $Y_0$  reference signal) input. It utilizes a slow and a fast counter to achieve the time resolution. Briefly, after appropriate frequency division, a phase-locked loop

<sup>43</sup> The CFDs use integration-differentiation type shaping, relying only on an RLC circuit, not delay lines. The CFD thresholds are controlled by software.

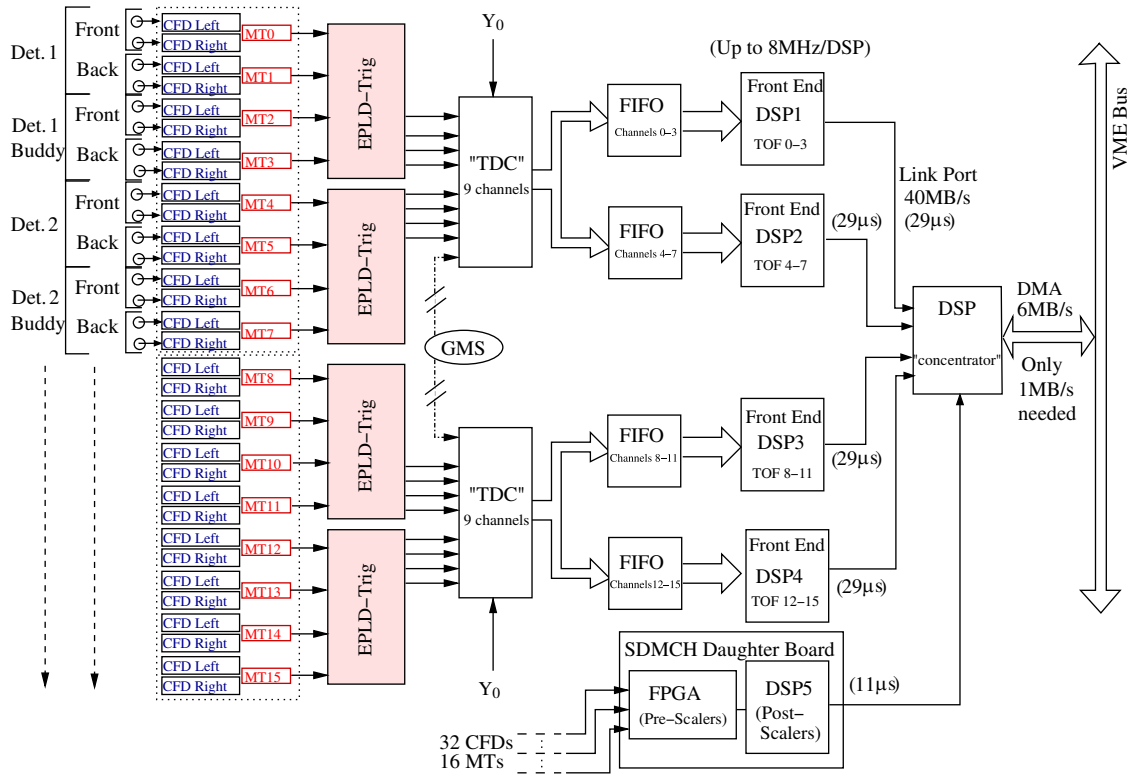


Fig. 19. Architecture of the FR DMCH boards for the forward angle measurement. Each board processes 32 PMT signals corresponding to eight pairs of scintillators.

is used to lock the frequency ( $\sim 250$  MHz) of a Voltage Control Oscillator (VCO) onto the  $Y_0$  signal. A slow counter running at the VCO frequency divides the 32 ns period of the  $Y_0$  signal into  $\sim 4$  ns periods. A fast counter consisting of eight delay-locked loop circuits then divides the 4 ns period into 16 bins of 250 ps. Once the time is flagged, the information is stored in one of the nine independent coding registers, and then transferred to the corresponding storage register using a synchronous FIFO buffer. The intrinsic deadtime of the time encoder is 24 ns and therefore does not introduce additional deadtime beyond that of the MT. Because of the design and the technology of the ASIC, the time encoder has a significant intrinsic differential non-linearity, which is corrected off-line.

In order to sustain a mean rate of a few MHz per channel (scintillator pair), the code of the four front-end DSPs is optimized so that a ToF bin is incremented using only four instructions (five cycles of 25 ns). Consequently, the maximum rate the DSP can handle is 8 MHz. As two such DSPs are associated with one time encoder in the normal coincidence mode of operation, the maximum rate per detector is 4 MHz.

Independent of the time-encoding data, an additional daughter board (SDMCH) containing an FPGA chip and a DSP provides individual scalers for the CFD and MT signals. Complementary to the Fastbus monitoring data, this scaler information helps in quantifying the deadtime associated with incomplete events, such as single CFD hits. The principle of these scalers is based on pre-scalers implemented on the FPGA chip and post-scalers collected by the SDMCH DSP.

At the end of each MPS, the four front-end DSPs and the SDMCH DSP rapidly transfer their data to the DSP concentrator through link ports (40 MB/s) working in parallel. This transfer takes  $29 \mu\text{s}$  during the  $500 \mu\text{s}$  dedicated to the beam helicity flip. The data transfer (5 kB) from the DSP concentrator to the ROC occurs during the next MPS using Direct Memory Access (DMA). At a rate of 6 MB/s, the transfer lasts 16 ms. Via the FR ROC, the

DMCH-16X data are gathered with the data from other ROCs in the CODA Event Builder. The total flow of the FR data is 1.4 MB/s which represents 2/3 of the total GO data transfer.

## 7.2. Backward angle electronics

For the backward angle measurements, a coincidence is formed between the signals from the FPDs and those from the CEDs mounted at the exit of the magnet, effectively determining the scattered electron momentum and angle, and thereby separating the elastic and inelastic electrons. Because ToF is not measured, the backward angle trigger is formed from a coincidence of the OR of all CEDs in an octant with an OR of the FPDs in the same octant. In addition to the signals from the CEDs and FPDs, Cherenkov detectors are employed, which generate a signal for the scattered electrons, but do not generate a signal from background  $\pi^-$ 's. The signal from the Cherenkov detector is therefore used to enable the coincidence logic. The required coincidences are performed in custom electronics using programmable logic devices. In contrast to the forward measurement, the coincidence rate is only  $\sim 100$  kHz for the elastic peak.

A summary of the basic logic in the backward angle electronics can be found in Fig. 20. The CED, FPD, and Cherenkov signals are combined to form the CED–FPD coincidences. Both coincidences with (electrons) and without (pions) the Cherenkov signal are recorded. Some data were also recorded (in the “pion” scalers) with the Cherenkov signal delayed by  $\sim 100$  ns to provide a direct measure of the random coincidences. The logic is also configured to reject events having more than one CED signal, or more than one FPD signal for a given beam burst. These multiple hit signals, as well as signals for both CED and FPD singles events are recorded to assist in deadtime loss and pile-up corrections. Again, implementations which differ in detail are adopted for the NA and FR octants, and they are described separately in the following.

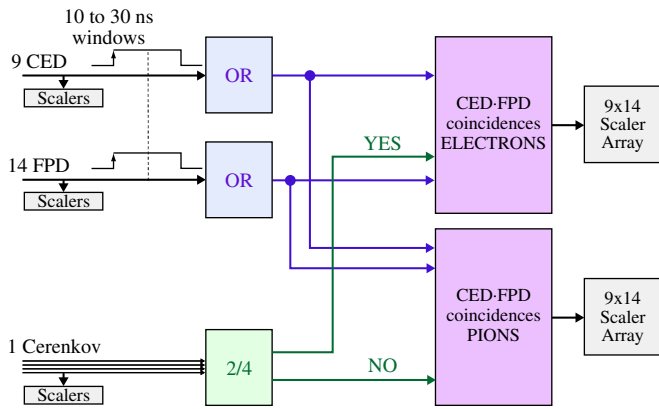


**Fig. 20.** Schematic and timing diagram for the backward angle electronics. The NA and FR layouts are similar, but with different components for the coincidence and scaler modules (see text).

### 7.2.1. NA electronics—backward angle

In the backward angle NA electronics, these logic functions are performed in a series of custom boards which replace the LTD boards used for the forward angle measurements. For each of the four NA octants, the outputs of the CED and FPD mean-timer modules are split, sending one copy to the scalers, and one copy to the main logic board. The main logic board performs the timing coincidence between the CEDs and FPDs, determines if a multiple hit event occurred, and sorts the coincidences according to which CED–FPD pair is hit. An Altera programmable logic device (PLD) [62] performs the logic functions. The CED–FPD coincidence information, for events without multiple hits, is then encoded into one 8-bit word, and sent on the crate back plane to a set of three custom boards which decode the information to a form suitable for scaler input.

In addition to the 8-bit word, one bit indicating the existence of a multiple hit event, and all CED and FPD singles events which had the correct timing, are sent on the back plane to another custom board which again uses a PLD to perform a coincidence between the CED and FPD correct-time singles events with the multiple hit bit.

The 8-bit word containing the CED–FPD coincidence information is taken from the back plane by the custom decoder boards and latched in another PLD to avoid timing jitter among the eight separate signals comprising the word. The Cherenkov signal is also used as an input to the decoder PLDs to release, as appropriate for electrons and for pions, the information through the latch. The 8-bit word is then decoded into individual CED–FPD coincidence signals, which are sent to the scalers for recording. To accommodate the four NA octants, a custom crate with four separate 5-slot back planes is employed.

### 7.2.2. FR electronics—backward angle

The FR electronics design for the backward angle measurement makes use of a part of the custom module developed for the forward angle measurement. As in the NA electronics, it is based on the coincidences between CED and the FPD detectors, enabled by the Cherenkov signal (corresponding to the detection of electrons); see Fig. 20. Each of the  $9 \times 14$  CED–FPD coincidences, for both the electron and pion cases, are then histogrammed during the MPS and transferred to the acquisition system during the helicity reversal time. The CFDs, mean-timers and scalers for the forward angle measurement are re-used, in conjunction with an additional VXI module based on an Altera PLD [62]. In a manner similar to that in the NA electronics, the logic board also provides capabilities for recording singles and multihit events used to characterize the deadtime.

## 7.3. Monitoring electronics

As described above, custom electronics are required to accumulate data at the very high rates needed to give sufficient statistics for precise measurement of the small asymmetries of interest in this experiment. The trade-off for making measurements at such high rates is that very little information can be recorded, as event-by-event recording is prohibitive (data transfer and recording rates). A separate set of conventional LeCroy Fastbus ADCs (1885F) and TDCs (1875A) [60] is used to capture much more detailed event-by-event information for a tiny fraction of the events. For the forward angle, the trigger used to start the TDCs and gate the ADCs is simply a pre-scaled version of the  $Y_0$  signal; in the backward angle case a conventional start/gate is provided based on the pre-scaled CED–FPD coincidence trigger described above. The pre-scale value is chosen to reduce the trigger rate to, typically, a few hundred Hz. During normal operation, the collection, digitization, and readout of a monitoring event takes about 1 ms.

Splitters are used to send a copy of each PMT signal to an ADC channel as well as sending it to the discriminator input. A copy of each CFD output is sent to a TDC channel, as is a copy of each mean-timer output. In addition, for the backward angle data, a simple wave form digitizer (“analog ring sampling” module) is used to monitor the analog signals from the individual Cherenkov PMTs. It samples the signals at 1 GHz over 128 ns for each monitoring event.

These monitor electronics make it possible to check the basic operation of the PMTs, discriminators and mean-timers. Furthermore, the correlated event-by-event information allows investigation of a wealth of effects which could not be seen with only the data from the main high-rate electronics. These include monitoring of the rate, time-distribution and pulse-height of single PMT hits (to check PMT gains, discriminator thresholds, etc.), single scintillator hits, etc.

## 7.4. Data-acquisition electronics

The G0 data-acquisition system is built on CODA [58], developed at Jefferson Lab. The electronics subsystems each occupy one or more crates, with triggering and event control performed by the Trigger Supervisor module and the Trigger Interface modules [63].

The standard event, monitoring, and GMS trigger sources are input to the Trigger Supervisor. It registers the arrival of the trigger signal, and begins processing the event. The trigger type information is passed to the other crates through a connection between the Trigger Supervisor and the Trigger Interface module in each crate. The DAQ software for each crate reads out individual modules depending upon the trigger type. For example, for monitor events, the Fastbus crate is read out through ROC 5, but ROCS 1–4 and the beam and control electronics are not read out.

As is mentioned in Section 7.3, the trigger source for the monitoring events is a pre-scaled copy of either the  $Y_0$  signal (forward angle) or coincidence signal (backward angle). It is pre-scaled in hardware to provide a trigger input rate of  $< 1$  kHz. There is an additional pre-scale in the Trigger Supervisor software; during typical operating conditions, the overall accepted trigger rate is a few hundred Hz.

We normally read out information at 30 Hz, following each MPS. In the 120 Hz over-sampling mode, there are two trigger types used: (A) which occurs at 30 Hz, and (B) which corresponds to the three additional 120 Hz phases between each MPS trigger. The FR electronics is read for type A; the NA for both type A and type B.

### 7.5. Data analysis

A brief description of the analysis system is given here to complete the overall description of the G0 apparatus. The main G0 replay code has, as input, a CODA file produced by the DAQ system. Its primary outputs are histograms and ntuples, filled on an “event-by-event” (MPS or QRT) basis, and a MySQL [64] database where only values averaged over a run (typically 1 h in duration) are saved. The database is used as the primary source for further analysis, whereas the histograms and ntuples are mainly used for analysis of calibration data. For each of the forward and backward angle runs, roughly 10 TByte of data are recorded in CODA files, and these raw data are subsequently reduced to a database of  $\sim 10$  GByte.

The main analysis treats the MPS (30 Hz) events which are of two types. For the forward angle measurement, the first type consists of ToF spectra associated with the FPDs (see Fig. 21); for the backward angle it comprises the matrix of CED–FPD coincidences (see Fig. 22). For both cases, the second type consists of beam diagnostic data, integrated over the 33 ms helicity window. These data include measurements of beam

current, energy, position and angle, and the data from the luminosity monitors.

The analysis of the 30 Hz data is based on the following procedure. For each MPS and for each ToF (forward) or coincidence (backward) channel, the yield ( $N$ ) is normalized by the beam charge accumulated during the MPS. The event is tagged as bad if the average beam current on target during its MPS is less than (typically)  $5 \mu\text{A}$ , or if the electronics associated with this detector has sent an error bit. The helicity state (which is encoded in the data stream with a delay of 8 MPS) of the beam is then decoded and associated with each MPS event. As discussed in Section 3.3, the beam helicity sequence is produced in a quartet structure of macropulses. The first MPS of each quartet is tagged in the data stream, and if the analysis has identified all four of the MPS in the quartet to be good, an asymmetry is computed for each channel

$$A(\text{quartet, time bin}) = \frac{\left(\frac{N_+^1 + N_+^2}{Q_+^1 + Q_+^2}\right) - \left(\frac{N_-^1 - N_-^2}{Q_-^1 - Q_-^2}\right)}{\left(\frac{N_+^1 + N_+^2}{Q_+^1 + Q_+^2}\right) + \left(\frac{N_-^1 - N_-^2}{Q_-^1 - Q_-^2}\right)} \quad (7)$$

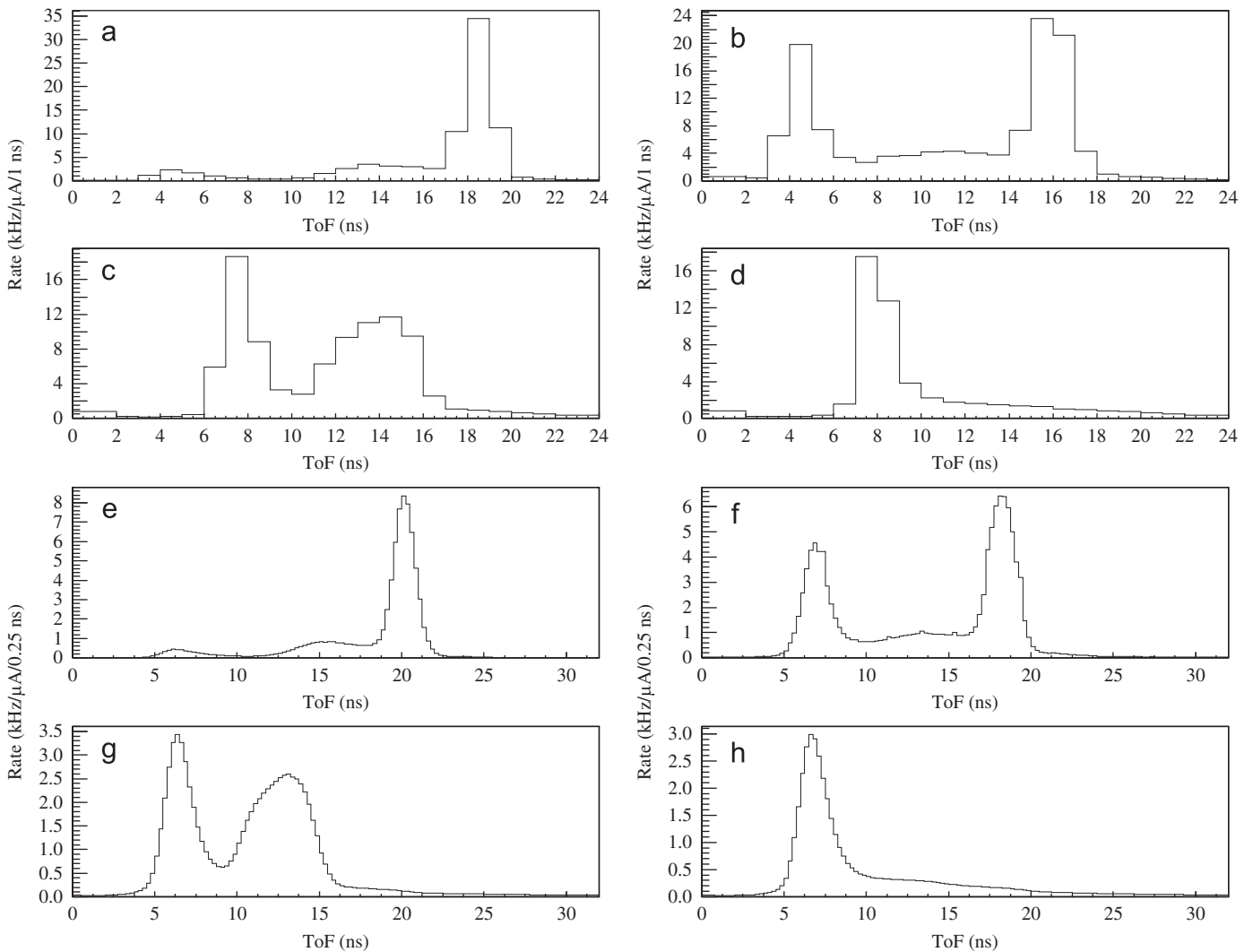


**Fig. 21.** Sample forward angle ToF spectra: (a) NA FPD 1, (b) NA FPD 11, (c) NA FPD 15, (d) NA FPD 16, (e) FR FPD 1, (f) FR FPD 11, (g) FR FPD 15, and (h) FR FPD 16 ( $t=0$  is slightly different for the NA and FR detectors). For detector numbers 1–14, the elastically scattered protons appear as a sharp peak at late ToF, while the pions appear at earlier ToF, with their measured rate increasing with increasing ring number. For detector 15, the elastically scattered protons appear as a broad distribution because the  $Q^2$  range of the acceptance of this ring is  $\sim 0.4 (\text{GeV}/c)^2$  compared to less than  $0.1 (\text{GeV}/c)^2$  for the other detectors. Finally, there is no acceptance for elastic events in detector 16, where only pions and inelastically scattered protons are measured. Note that for  $24 < t < 32$  ns, for which we recorded information only with the FR electronics, the count rate is negligible.

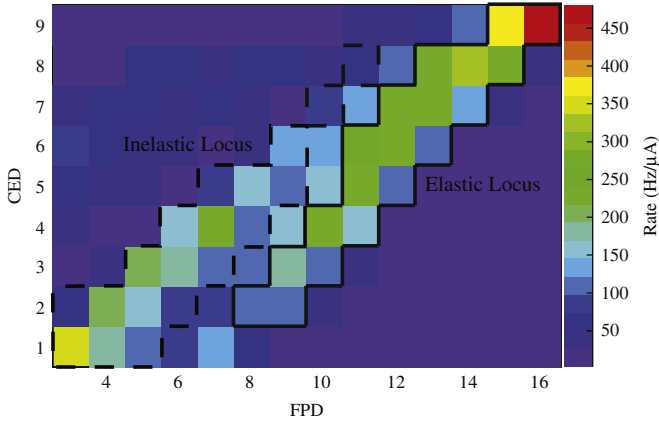


**Fig. 22.** Backward angle measurement of scattered electrons from the LH<sub>2</sub> target at 684 MeV incident energy, showing coincidence rates for the various combinations of CEDs and FPDs. The elastically scattered electrons appear in a band toward the upper right, the inelastically scattered electrons in a band toward lower left as shown.

where  $N_s^i$  is the number of counts recorded for the  $i$ th MPS of this quartet with beam helicity of sign  $s$ , and  $Q_s^i$  is the beam charge incident on target during this MPS. If one or more of the MPS of the quartet is tagged as bad, the quartet is not included in the main run-averaged information. The asymmetries for a given target/angle combination are multiplied by a blinding factor (0.75–1.25) at this stage, and “unblinded” at the completion of the analysis.

For each channel, the asymmetry, as computed above, is averaged over the run with an uncertainty given by the root mean square deviation of the asymmetries over the run divided by the square root of the number of good macropulses for that channel. These values are saved in the database. Beam charge asymmetries and beam position differences are computed following the same algorithm of quartet identification and averaged for a run.

Corrections for three main effects, counting rate, helicity-correlated beam changes and backgrounds, are also computed in the analysis software. The rate corrections, both for deadtime and for random triggers are electronics-dependent and therefore different for the FR and the NA data [30,65]. Measured electronics busy fractions are combined with concurrent measurements of singles rates and asymmetries to make corrections to the raw asymmetry. These corrections typically amount to a few percent of the measured asymmetries.

Forming asymmetries using rate-corrected yields constitutes a “first-pass” analysis. During this pass, the sensitivity of each detector channel to variations in the beam position, angle, energy and current (the “yield slopes”  $\partial Y/\partial P_i$ , see Section 3.2) are also computed. In a second pass through the analysis, the detector yields  $N_s^i$  are corrected using these yield slopes and the corresponding, measured, helicity-correlated beam properties, prior to re-computing the asymmetry (Eq. (7)). It should be noted that the correction for yield variation as a function of the helicity-correlated beam current changes is small, both because the beam current changes themselves are small and because the first-order effects have already been removed by the (helicity-averaged) rate corrections.

An example of the resulting distribution of the QRT asymmetries for one FPD pair (for the entire forward angle measurement) is shown in Fig. 23, showing the expected Gaussian distribution with no tails. The expected width of this distribution can be computed from the measured count rate, after correction for deadtime effects [66]; Fig. 24 shows the ratio of the standard deviation of the measured distribution (forward angle) to that

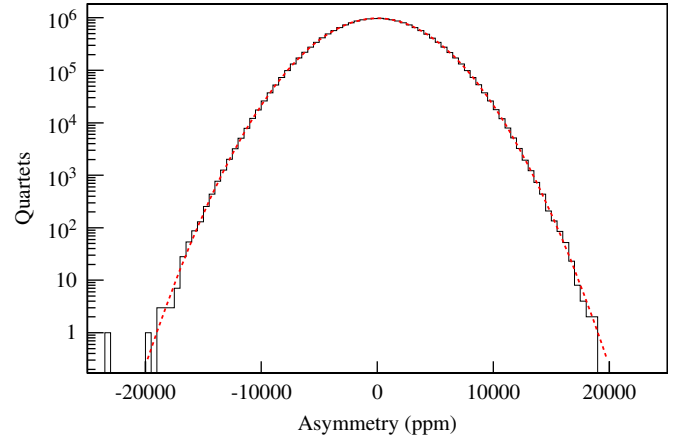


**Fig. 23.** The distribution of the measured forward angle, octant 7, FPD 8 proton asymmetries ( $1.7 \times 10^7$  quartets) together with a Gaussian fit ( $\chi^2/\nu = 84.2/74$ ).

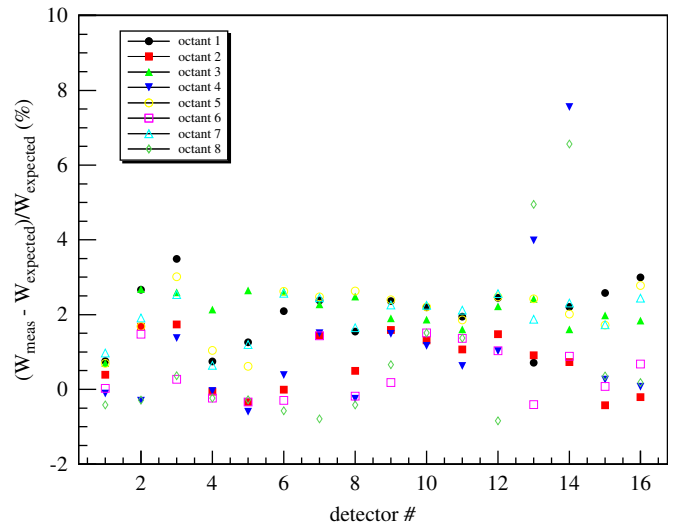


**Fig. 24.** The percentage difference between the measured and statistically expected forward angle proton asymmetry widths for all FPDs in all octants.

expected from the rates. We measure a distribution only  $\sim 2\%$  broader than that expected from counting statistics. As discussed in Section 4.4, a broadening of the width of order 1–2% is expected due to target density fluctuations. The few detectors with somewhat larger widths are likely either due to some additional electronic noise or an underestimate of the electronic deadtime. Neither effect is expected to be helicity-correlated, so would not introduce a systematic error, only a modest decrease in the statistical precision.

Finally, starting from the run-averaged information contained in the database, corrections for backgrounds are made using both the yield and asymmetry data, typically from neighboring channels and/or different triggers acquired concurrently with the main data.

## 8. Summary and operation history

The major components of the G0 experiment have been described. In addition to the experiment-specific hardware provided by the collaboration, such as the superconducting toroidal spectrometer, cryogenic target, and detector system, we have

provided a description of the polarized electron beam produced by the CEBAF accelerator.

The G0 experiment was first installed in Hall C of Jefferson Lab during the period July 2002 to October 2002. The first commissioning run took place over the next three months. In addition to commissioning the various hardware components associated with the experiment, significant time was spent by the accelerator group developing the specialized beam required by the G0 experiment; i.e., the modified time structure, the high beam current with the corresponding large beam bunch charge, and the required small helicity-dependent beam properties.

The G0 experiment was reinstalled, aided by the fact that the toroidal magnet and detector system were mounted on rails for easy installation and removal, during the Fall of 2003. Another commissioning/engineering run followed installation. The actual production runs for the forward angle measurement began about mid-March 2004 and continued until about May 2004, at which time the statistical goals of the experiment had been met. The results of the forward angle run have been published as a letter [5]. A longer paper providing details is in preparation.

Having completed the forward angle measurement, the new hardware for the back angle measurements was installed in Hall C, and commissioning and initial data-taking took place in March–May of 2006. A long period of production running followed—including measurements with both hydrogen and deuterium targets, each at beam energies of 359 and 684 MeV—ending in April 2007. The results of the main backward angle electron asymmetry measurements have been published [6]; a longer paper providing details about this phase of the experiment is also in preparation.

## Acknowledgments

This work is supported in part by grants from several agencies. The U.S. DOE provided support for the construction of the North American detectors, the North American electronics, for the infrastructure and operation of Jefferson Lab, as well as for the activities of some collaborating groups. The U.S. NSF provided funding for the superconducting magnet and the cryogenic target, as well as for the activities of some collaborating groups. The French CNRS provided support for the French detectors and electronics, as well as for the activities of the French collaborators. The Canadian NSERC provided support for the North American detectors and electronics as well as for the activities of the Canadian groups. We thank all the funding agencies for their support to the experiment.

We would like to thank the administration and staff of Jefferson Laboratory, especially members of the Accelerator and Hall C groups who made strong contributions to the success of the experiment. We would also like to acknowledge the contributions of, and to thank the technical staff at Caltech (target), Carnegie Mellon (detectors, electronics), Grenoble (detectors, electronics), Illinois (magnet), Orsay (detectors, electronics), and TRIUMF (detectors, magnet).

## References

- [1] D.H. Beck, R.D. McKeown, *Ann. Rev. Nucl. Part. Sci.* 51 (2001) 189.
- [2] R.D. McKeown, *Phys. Lett. B* 219 (1989) 140.
- [3] D.H. Beck, *Phys. Rev. D* 39 (1989) 3248.
- [4] G.A. Miller, *Phys. Rev. C* 57 (1998) 1492; B. Kubis, R. Lewis, *Phys. Rev. C* 74 (2006) 015204.
- [5] D.S. Armstrong, et al., G0 Collaboration, *Phys. Rev. Lett.* 95 (2005) 092001.
- [6] D. Androić, et al., G0 Collaboration, *Phys. Rev. Lett.* 104 (2010) 012001.
- [7] S.D. Covrig, et al., *Nucl. Instr. and Meth. A* 551 (2005) 218.
- [8] D. Marchand, et al., *Nucl. Instr. and Meth. A* 586 (2008) 251.
- [9] E.J. Beise, M.L. Pitt, D.T. Spayde, *Prog. Nucl. Part. Phys.* 54 (2005) 289.
- [10] See, for example, A. Acha, et al., *Phys. Rev. Lett.* 98 (2007) 032301.
- [11] C.K. Sinclair, et al., *Phys. Rev. ST Accel. Beams* 10 (2007) 023501.
- [12] Bandwidth Semiconductor, LLC. <[www.spirecorp.com/spire-bandwidth-semiconductor/](http://www.spirecorp.com/spire-bandwidth-semiconductor/)>.
- [13] T. Maruyama, et al., *Appl. Phys. Lett.* 85 (2004) 2640.
- [14] C.W. Leemann, D.R. Douglas, G.A. Krafft, *Ann. Rev. Nucl. Part. Sci.* 51 (2001) 413.
- [15] Time Bandwidth Products <[www.tbwp.com](http://www.tbwp.com)>.
- [16] Jefferson Lab experiment E94-107, S. Frullani, F. Garibaldi, J. LeRose, P. Markowitz, T. Saito, spokespersons.
- [17] R. Kazimi, et al., in: *Proceedings of the 9th European Accelerator Conference (EPAC 2004)* <<http://accelconf.web.cern.ch/AccelConf/e04/>>, JLAB-ACO-04-251.
- [18] W. Barry, *Nucl. Instr. and Meth. A* 301 (1991) 407.
- [19] T. Powers, L. Doolittle, R. Ursic, J. Wagner, in: *Proceedings of the 7th Workshop on Beam Instrumentation*, AIP Conf. Proc. 390 (1997) JLAB-TN-96-021.
- [20] R.A. Mair, et al., *Phys. Lett. A* 212 (1996) 231.
- [21] K.A. Aniol, et al., HAPPEX Collaboration, *Phys. Rev. C* 69 (2004) 065501.
- [22] K. Nakahara, in: S. Kox, D. Lhuillier, F. Maas, J. van de Wiele (Eds.), *Proceedings of the International Workshop on Parity Violation and Hadronic Structure (PAVIO4)*, *Eur. Phys. J.* 24 (2005) s2.119.
- [23] K. Nakahara, Ph.D. Thesis, University of Illinois, 2006, G0-doc-657.
- [24] M. Hauger, et al., *Nucl. Instr. and Meth. A* 462 (2001) 382.
- [25] S. Phillips, Ph.D. Thesis, College of William and Mary, 2009, G0-doc-841.
- [26] J. Grames, et al., *Phys. Rev. ST Accel. Beams* 7 (2004) 042802.
- [27] J.S. Price, et al., in: N.E. Tyurin, V.L. Solovianov, S.M. Troshin, A.G. Ufimtsev (Eds.), *Proceedings of the 13th Symposium on High Energy Spin Physics (SPIN98)*, Protvino, Russia, 1998, World Scientific, Singapore, 1999.
- [28] X. Yan, N. Sinkine, R. Wojcik, *Nucl. Instr. and Meth. A* 539 (2005).
- [29] EPICS: Experimental Physics and Industrial Control System <<http://www.aps.anl.gov/epics/>>.
- [30] J. Liu, Ph.D. Thesis, U. Maryland, 2006, G0-doc-650.
- [31] S.D. Covrig, Ph.D. Thesis, Caltech, 2004, G0-doc-483.
- [32] Barber-Nichols Engineering Co. <[www.barber-nichols.com](http://www.barber-nichols.com)>.
- [33] Thermionics <[www.thermionics.com](http://www.thermionics.com)>.
- [34] Lakeshore Cryotronics, Inc. <[www.lakeshore.com](http://www.lakeshore.com)>.
- [35] K.L. Brown, *Adv. Part. Phys.* 1 (1967) 71.
- [36] Jefferson Lab experiment E97-104, S.P. Wells, N. Simicevic, spokespersons, G0-doc-198.
- [37] Now Babcock and Wilcox Technical Services Group <[www.babcock.com/about/business\\_units/technical\\_services\\_group](http://www.babcock.com/about/business_units/technical_services_group)>.
- [38] P.D. Brindza, et al., *IEEE Trans. Appl. Superconductivity* 16 (2006) 248.
- [39] MFA 906 + Al, available through The Doer Run Co. <[www.doerun.com](http://www.doerun.com)>.
- [40] Titanium Metal Corporation <[www.timet.com](http://www.timet.com)>.
- [41] Dynapower Corporation <[www.dynapower.com](http://www.dynapower.com)>.
- [42] Sécheron SA <[www.secheron.com](http://www.secheron.com)>.
- [43] Post Glover <[www.postglover.com](http://www.postglover.com)>.
- [44] W. Falk, et al., *Magnetic verification of the G0 superconducting magnet system*, TRIUMF Annual Report, 2002.
- [45] G. Batigne, Ph.D. Thesis, Université Joseph Fourier—Grenoble, 2004, G0-doc-478.
- [46] Automation Direct <[www.automationdirect.com](http://www.automationdirect.com)>.
- [47] C. Drennan, CDF Solenoid Interlocks Component Failure Analysis, December 6, 1999, unpublished.
- [48] R. Hance, Solenoid quench protection system single device failure analysis, FNAL Engineering Note H971203B, Revised January 21, 1998.
- [49] R. Tieulent, Ph.D. Thesis, Université Joseph Fourier—Grenoble, 2002, G0-doc-321.
- [50] OPERA-3D, Cobham Technical Services <[www.cobham.com](http://www.cobham.com)>.
- [51] Now Saint-Gobain Ceramics and Plastics <[www.bicrondirect.com](http://www.bicrondirect.com)>.
- [52] Photonis <[www.photonis.com](http://www.photonis.com)>.
- [53] D.W. Higinbotham, *Nucl. Instr. and Meth. A* 414 (1998) 332.
- [54] See, for example, H. Tanaka, Masters Thesis, Tokyo Institute of Technology, 2002, unpublished.
- [55] Bosch Aluminum Structural Framing System <[www.boschrexroth.com](http://www.boschrexroth.com)>.
- [56] Matsushita Electric Works <[www.mew.co.jp/e-aerogel](http://www.mew.co.jp/e-aerogel)>.
- [57] Millipore Corporation <[www.millipore.com](http://www.millipore.com)>.
- [58] W.A. Watson, et al., in: *Proceedings of the Real Time 1993 Conference*, p. 296; G. Heyes, et al., in: *Proceedings of the CHEP Conference*, 1994, p. 122; D.J. Abbott, et al., in: *11th IEEE NPSS Real Time 1999 Conference*, JLAB-TN-99-12; <[coda.jlab.org](http://coda.jlab.org)>.
- [59] J. Musson, T. Allison, A. Freyberger, J. Kuhn, B. Quinn, *Nucl. Instr. and Meth. A* 540 (2005) 448.
- [60] Formerly LeCroy Research Systems <[www.lecroy.com/lrs](http://www.lecroy.com/lrs)>.
- [61] Analog Devices Inc. <[www.analog.com](http://www.analog.com)>.
- [62] Altera Corp. <[www.altera.com](http://www.altera.com)>.
- [63] E. Jastremski, et al., The Jefferson Lab trigger supervisor system, in: *11th IEEE NPSS Real Time 1999 Conference*, JLAB-TN-99-13, 1999.
- [64] MySQL <[www.mysql.com](http://www.mysql.com)>.
- [65] M. Versteegen, Ph.D. Thesis, Université Joseph Fourier—Grenoble, 2009, G0-doc-854.
- [66] B. Guillon, Ph.D. Thesis, Université Joseph Fourier—Grenoble, 2005, G0-doc-619.